Report

Cell Reports

Removing 4E-BP Enables Synapses to Refine without Postsynaptic Activity

Graphical Abstract

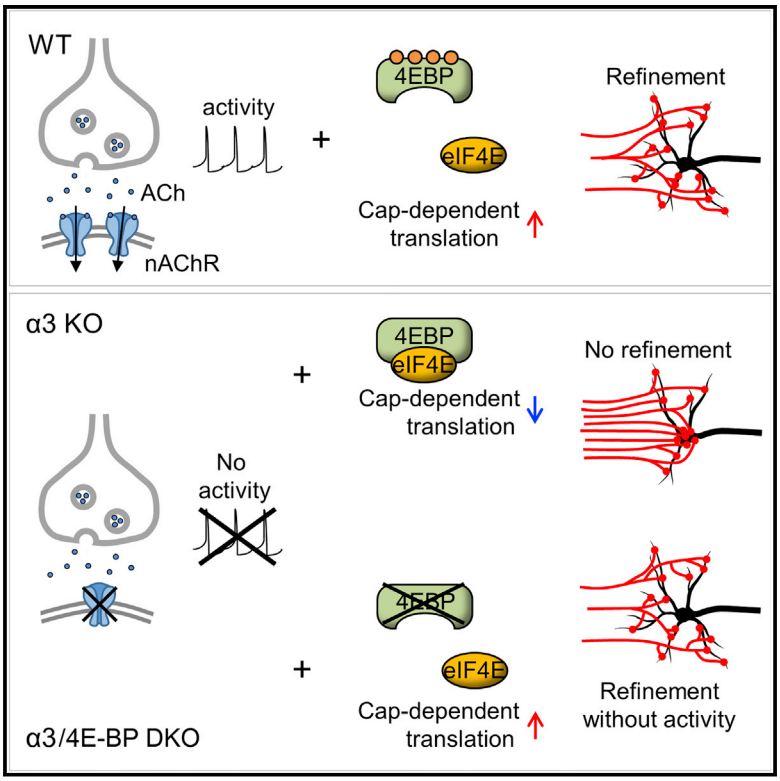

Authors

Yumaine Chong, Natasha Saviuk, Brigitte Pie, ..., Nahum Sonenberg, Ellis Cooper, A. Pejmun Haghighi

Correspondence

ellis.cooper@mcgill.ca (E.C.), phaghighi@buckinstitute.org (A.P.H.)

In Brief

Synaptic activity is required for synaptic refinement and reorganization during post-natal development. Chong et al. find that silent synapses in superior cervical ganglia (SCG) refine when 4E-BP is genetically removed, suggesting that enhanced cap-dependent translation promotes synaptic refinement in the absence of postsynaptic activity.

Highlights

- Postsynaptic activity regulates synaptic refinement at the SCG
- Postsynaptic activity influences 4E-BP phosphorylation in the SCG
- Loss of postsynaptic activity alters the proteomic profile of the SCG
- In the absence of postsynaptic activity, removal of 4E-BP restores synaptic refinement

Data and Software Availability

PXD007141

Chong et al., 2018, Cell Reports *23*, 11–22
April 3, 2018
https://doi.org/10.1016/j.celrep.2018.03.040

CellPress

Cell Reports
Report

Removing 4E-BP Enables Synapses to Refine without Postsynaptic Activity

Yumaine Chong,[1] Natasha Saviuk,[1] Brigitte Pie,[1] Nathan Basisty,[3] Ryan K. Quinn,[3] Birgit Schilling,[3] Nahum Sonenberg,[2] Ellis Cooper,[1,*] and A. Pejmun Haghighi[1,3,4,*]
[1]Department of Physiology, McGill University, Montreal, QC H3G 1Y6, Canada
[2]Department of Biochemistry, McGill University, Montreal, QC H3G 1Y6, Canada
[3]Buck Institute for Research on Aging, Novato, CA 94945, USA
[4]Lead Contact
*Correspondence: ellis.cooper@mcgill.ca (E.C.), phaghighi@buckinstitute.org (A.P.H.)
https://doi.org/10.1016/j.celrep.2018.03.040

SUMMARY

Throughout the developing nervous system, considerable synaptic re-organization takes place as postsynaptic neurons extend dendrites and incoming axons refine their synapses, strengthening some and eliminating others. It is well accepted that these processes rely on synaptic activity; however, the mechanisms that lead to this developmental reorganization are not fully understood. Here, we explore the regulation of cap-dependent translation, a mechanism known to play a role in synaptic growth and plasticity. Using sympathetic ganglia in α3 nicotinic acetylcholine receptor (nAChR)-knockout (KO) mice, we establish that electrophysiologically silent synapses between preganglionic axons and postsynaptic sympathetic neurons do not refine, and the growth of dendrites and the targeting of synapses on postsynaptic neurons are impaired. Remarkably, genetically removing 4E-BP, a suppressor of cap-dependent translation, from these α3 nAChR-KO mice largely restores these features. We conclude that synaptic connections can re-organize and refine without postsynaptic activity during post-natal development when 4E-BP-regulated cap-dependent translation is enhanced.

INTRODUCTION

During early post-natal development, as circuits begin to form, the emergent synaptic activity remodels axons and dendrites to refine synaptic connections and improve circuit performance. This activity-dependent refinement occurs widely in the developing nervous system (Purves and Lichtman, 1980; Sanes and Lichtman, 1999; Katz and Crowley, 2002; Bleckert and Wong, 2011; Hong and Chen, 2011; Buffelli et al., 2002; Zou et al., 2004; Schlaggar et al., 1993; Takeuchi et al., 2014; Yasuda et al., 2011), suggesting that this refinement is regulated by common mechanisms; however, in spite of its widespread occurrence, the underlying mechanisms are not fully understood. It is generally accepted that synaptic refinement takes place through an activity-dependent competitive process(es) that eliminates some inputs and strengthens others (Cohen-Cory, 2002; Lichtman and Colman, 2000; Katz and Shatz, 1996; Zhang and Poo, 2001; Kano and Hashimoto, 2009). And, interfering with pre- or postsynaptic activity in developing circuits or manipulating postsynaptic calcium influx prevents inputs from refining (Fitzsimonds and Poo, 1998; Balice-Gordon and Lichtman, 1994; Hata and Stryker, 1994; Hashimoto et al., 2011), indicating clearly that the processes that lead to synaptic refinement require activity. Given recent evidence that activity-dependent mechanisms promote cap-dependent mRNA translation in developing dendrites and axons and play essential roles in forming neural circuits (Bramham and Wells, 2007; Lin et al., 2016; Jung et al., 2012; Wang et al., 2010), we asked whether cap-dependent translation has any role in re-organizing neural connections during post-natal development.

Briefly, a critical step in regulating cap-dependent translation is binding of the eukaryotic translation initiation factor 4E (eIF4E) to the 5′ cap structure of mRNAs (Gingras et al., 1999; Sonenberg and Hinnebusch, 2009). The availability of eIF4E is controlled by 4E-binding proteins (4E-BPs), important regulators of cap-dependent mRNA translation and major downstream targets of the mechanistic target of rapamycin complex 1 (mTORC1), a serine-threonine kinase (Richter and Sonenberg, 2005; Thoreen et al., 2012). Hypophosphorylated 4E-BP represses the initiation of cap-dependent translation by sequestering eIF4E, whereas hyperphosphorylated 4E-BP releases eIF4E and allows eIF4E to bind to eIF4G, a molecular interaction that is required to initiate cap-dependent translation and *de novo* protein synthesis (Gingras et al., 1999; Sonenberg and Hinnebusch, 2009).

To determine whether cap-dependent translational mechanisms have a role in synaptic refinement during post-natal development, we investigated synapses in the superior cervical ganglion (SCG), a well-established model that is known to undergo considerable synaptic reorganization and refinement during the first post-natal month as circuits are being established (Purves and Lichtman, 1984). Briefly, all SCG neurons are innervated exclusively by a homogeneous group of excitatory cholinergic preganglionic axons that are anatomically well defined and readily accessible for stimulation and labeling. Moreover, SCG neurons receive no other excitatory innervation,

nor do they receive inhibitory innervation; therefore, refinement of preganglionic axons is not confounded by other inputs to the postsynaptic neurons. Furthermore, fast synaptic transmission between preganglionic axons and sympathetic neurons in the SCG is mediated by only 1 class of postsynaptic receptors: α3-containing nicotinic acetylcholine receptors (nAChRs) (Xu et al., 1999; Rassadi et al., 2005). Therefore, deleting the α3 nAChR subunit gene from mice (referred to here as α3 knockout [KO]) completely abolishes synaptic transmission in the SCG (Rassadi et al., 2005; Krishnaswamy and Cooper, 2009), even though the presynaptic terminals establish synapses that appear ultrastructurally normal (Krishnaswamy and Cooper, 2009). In addition, one can rapidly restore function to these synapses by infecting postsynaptic neurons with α3-expressing adenoviruses (Krishnaswamy and Cooper, 2009).

Using α3-KO mice of different post-natal ages, we show that SCG neurons remain innervated by multiple preganglionic axons and we find defects in the growth of dendrites on α3-KO sympathetic neurons and in the targeting of synapses by preganglionic axon terminals. Un-silencing these synapses by virally introducing α3 normalized synaptic targeting to dendrites, and enabled the preganglionic axons to refine. In α3-KO sympathetic neurons, we found lower levels of phosphorylated 4E-BP1 compared to that in wild-type (WT) controls. Additionally, in proteomic experiments, we observed changes in levels for a large number of proteins in the SCG of α3-KO mice. Interestingly, genetically removing 4E-BP from α3-KO mice largely restored these protein levels toward those in WT, even though the SCG had no synaptic transmission. Furthermore, we show that removing 4E-BP from α3-KO mice reversed the defects both in dendritic growth on SCG neurons and in targeting of synapses, and, remarkably, the preganglionic inputs refined in the absence of postsynaptic activity. Our findings highlight a role for cap-dependent translation in re-organizing connections, particularly in circuits where synapses have been silenced.

RESULTS

The Absence of Preganglionic Refinement in the SCG of α3-KO Mice

To estimate the number of preganglionic synaptic inputs onto sympathetic neurons in WT SCG, we measured the discrete jumps in the evoked excitatory postsynaptic potentials (EPSPs) while gradually increasing the stimulus to the preganglionic nerve to recruit innervating axons (Figure 1). In post-natal day 1–3 (P1–P3) mice, approximately 7–8 preganglionic axons converged onto postsynaptic sympathetic neurons, each axon evoking a small EPSP of approximately equal strength (Figure 1A). Over the first post-natal month, as neonatal pups start to regulate internal organs to maintain homeostasis, activity in the autonomic nervous system increases dramatically and some preganglionic axons innervating sympathetic neurons are gradually eliminated. By P8–P9, sympathetic neurons were innervated by approximately 5–6 axons, and, by P28–P30, only 2–3 axons innervated SCG neurons (Figures 1B and 1F). In addition, over this time period, the strength of the inputs had increased markedly. At P56–P64, the neurons remained innervated by 2–3 axons (Figure 1F).

We quantified the disparity in strength of the EPSPs on each neuron in two ways. In one, we calculated a disparity index, defined as the ratio of the SD of the EPSPs evoked by each axon divided by the mean (SD/M) (Hashimoto and Kano, 2003; see the Experimental Procedures and Supplemental Information). From P1–P3 to P28–P30, we observed a significant increase in the mean disparity index (DI) (Figures 1A and 1B), reflecting the increase in strength of 1 or more inputs. In the second method, we computed the difference in strength between the strongest and second strongest inputs, expressed as a percentage of the maximum compound EPSP. At P1–P3, the difference between the strongest and the next strongest input was <5%, whereas at P28–P30 the difference was ~35% (Figure 1E). These results establish that, over the first post-natal month, preganglionic inputs innervating sympathetic neurons refine their connections by eliminating some axons and strengthening others.

To test whether refinement is dependent on synaptic activity, as it is elsewhere in the nervous system (Lichtman and Colman, 2000; Katz and Shatz, 1996; Zhang and Poo, 2001), we examined preganglionic innervation in the SCG of post-natal α3-KO mice. Synapses are electrophysiologically silent in the SCG when α3-containing nAChRs are absent, although synapses are morphologically intact (Krishnaswamy and Cooper, 2009). We first infected these mice for 1–2 days with α3-encoding adenoviral vectors (Ad-α3) so that we could measure the convergence of preganglionic axons. At P1–P3, approximately 7–8 preganglionic axons converged onto postsynaptic sympathetic neurons, with each axon evoking a small EPSP of approximately equal strength (Figure 1C), comparable to that of WT at P1–P3. In contrast to WT, preganglionic axons innervating α3-KO SCG neurons showed no refinement, and the neurons continued to be innervated by 7–8 axons over the next 2 months of post-natal life (Figures 1D and 1F). Moreover, EPSPs measured from α3-KO neurons showed little disparity during the same period of time (Figures 1D and 1E). These results suggest that postsynaptic activity during the first post-natal month is necessary both for the elimination of some preganglionic axons and the strengthening of those inputs that persist.

Preganglionic Axons Refine when Synaptic Activity Is Restored in α3-KO SCG

To examine whether preganglionic axons in α3-KO mice are capable of refining when postsynaptic activity is restored, we infected mice with Ad-α3 at P28–P30, and we examined functional innervation of SCG neurons 1 month later (at P56–P64). We found that rescued α3-KO SCG neurons were innervated by only 2–3 preganglionic axons (Figure 2A), similar to that of WT neurons at P60 (Figure 2C), whereas α3-KO SCG neurons (not rescued) at P60 continued to be innervated by 7–8 axons (Figure 2B). In addition to the shift in convergence, the EPSPs evoked by 1–2 preganglionic axons on rescued neurons strengthened considerably, increasing the disparity among EPSPs to levels in WT SCG (Figures 2A, 2C, and 2D). From these data, we conclude that, to refine and strengthen, synapses made

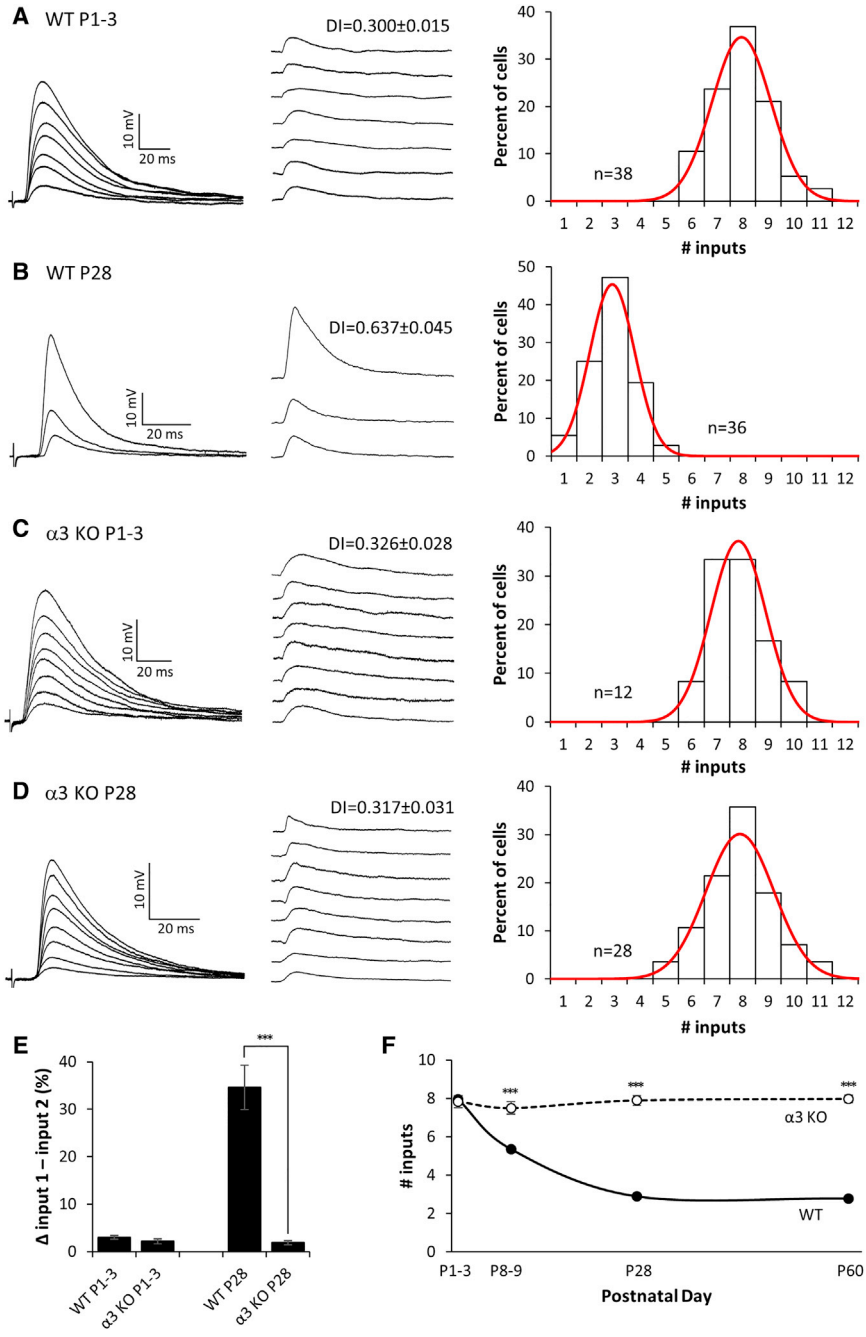

Figure 1. Preganglionic Axons Innervating Neurons in α3-KO SCG Do Not Refine

(A–D) Left: representative compound EPSPs in an SCG neuron from (A) P1–P3 WT, (B) P28 WT, (C) P1–P3 α3-KO, and (D) P28 α3-KO mice evoked by increasing stimuli to the preganglionic nerve. Middle: the EPSPs evoked by individual preganglionic axons are shown. DI, disparity index. Right: distribution of SCG neurons innervated by the number of inputs; each distribution was fit with a Gaussian function. The distribution for P28 α3 KO is not significantly different from P1–P3 WT or α3 KO ($p > 0.2$), but it is significantly different from P28 WT ($p < 0.001$). Each distribution in (A)–(D) contains data from at least 4 mice. n, number of neurons.

(E) The average difference in strength between the strongest and second strongest inputs, expressed as a percentage of the maximum compound EPSP.

(F) The average number of axons innervating an SCG neuron in WT (solid line) and α3-KO (dotted line) mice at P1, P4, P28, and P60.

For (E) and (F), error bars represent ± SEM. ***$p < 0.001$.

by preganglionic axons require retrograde signals downstream of postsynaptic activity. Furthermore, our findings demonstrate that presynaptic inputs onto postsynaptic sympathetic neurons maintain their ability to refine in an activity-dependent manner, well beyond the post-natal period.

The Extension of Dendrites and Targeting of Synapses Are Defective in the Absence of Postsynaptic Activity

In addition to the convergence of preganglionic axons, we asked whether the absence of postsynaptic activity modifies the organization of pre- and postsynaptic structures, including the growth of dendrites, and/or the manner in which preganglionic axons target their synapses onto SCG neurons.

To quantify dendritic growth, we sparsely labeled SCG neurons with the lipophilic dye 3,3′-Dioctadecyloxacarbocyanine perchlorate (DiO). At P1, total dendritic outgrowth (TDO) on WT and α3-KO neurons was similar (Figures 3A–3C); however, TDO on WT neurons was significantly greater than that on α3-KO neurons by as early as P4, and, by P28, TDO on WT neurons was twice that of α3-KO neurons (Figures 3A–3C). These results are consistent with a role for activity in promoting dendritic growth (Haas et al., 2006; Niell et al., 2004; Wong and Ghosh, 2002; Cline, 2001). The main defect in dendritic growth on sympathetic neurons developing without excitatory synaptic transmission was that they could not maintain primary branches (Figure 3D): the number of primary dendrites on α3-KO neurons decreased from five at P1–P4 to three at P28. On the other hand, we found no significant difference in the length of the dendritic branches on α3-KO neurons compared to neurons in WT SCG, nor did we find differences in the number of secondary or higher-order branches, once normalized for primary branch number (Figure 3E; Figure S1). These results suggest that, apart from maintaining primary dendrites, most aspects of dendritic growth on sympathetic neurons do not depend on synaptic activity.

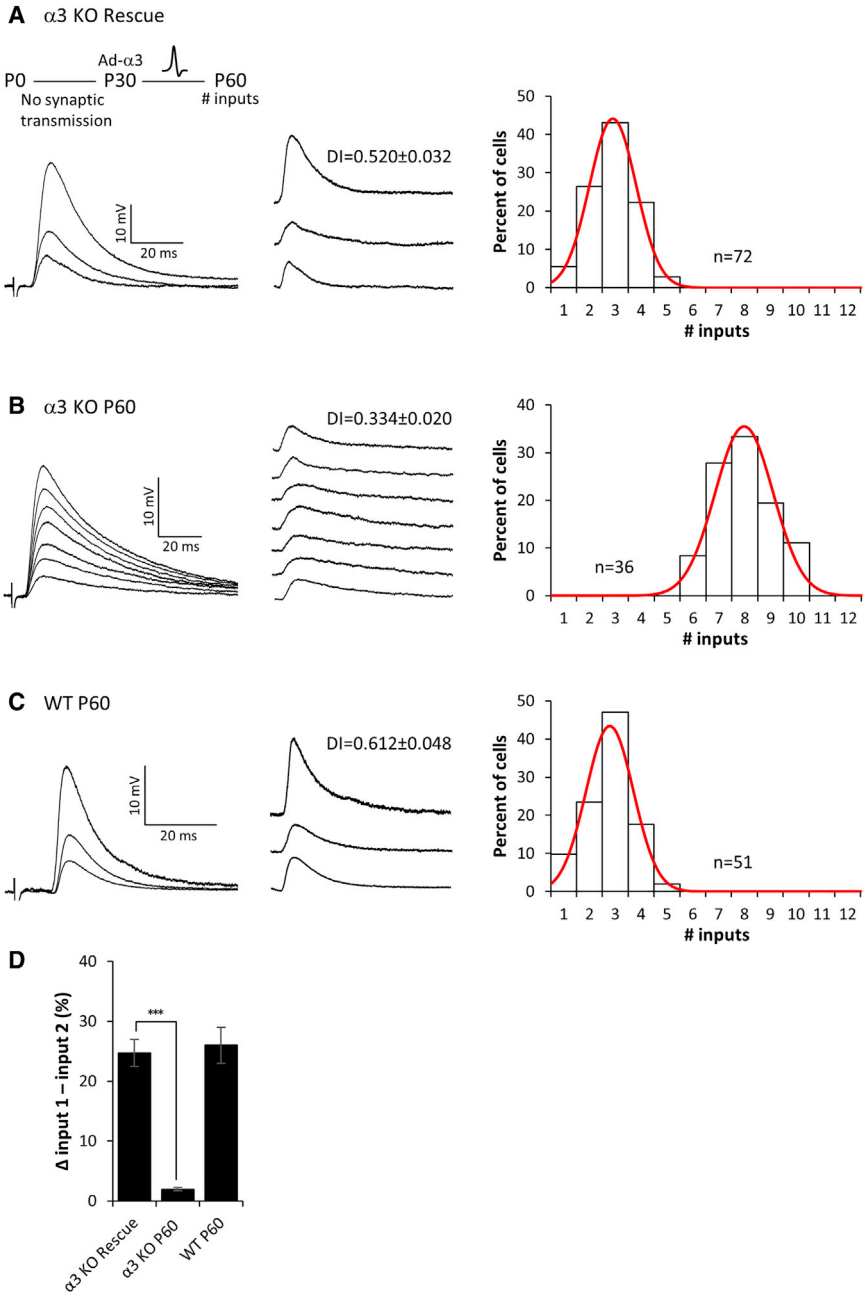

Figure 2. Refinement of Preganglionic Axons Requires Postsynaptic Activity

(A–C) Left: representative compound EPSPs evoked in an SCG neuron from (A) α3-KO mice 1 month after rescue (see inset), (B) P60 α3-KO mice, and (C) P60 WT mice. Middle: the EPSPs evoked by individual preganglionic axons are shown. DI, disparity index. Right: distribution of the SCG neurons innervated by the number of inputs; each distribution is fit with a Gaussian function. The distribution for α3-KO rescue neurons is not significantly different from P60 WT ($p > 0.2$), but it is significantly different from P60 α3 KO ($p < 0.001$). Each distribution in (A)–(C) contains data from at least 4 mice. n, number of neurons. (D) The average difference in strength between the strongest and second strongest inputs, expressed as a percentage of the maximum compound EPSP. Error bars represent ± SEM. ***$p < 0.001$.

Preganglionic axons mainly target their synapses to the dendrites of sympathetic neurons (Forehand, 1985). Given the decrease in primary dendrites when synaptic transmission is absent, we asked whether preganglionic axons targeted their synapses differently on α3-KO and WT SCG neurons. To address this, we sparsely labeled preganglionic axons in WT and α3-KO SCG at P28 with 1,1′-Dioctadecyl-3,3,3′,3′-tetramethylindocarbocyanine perchlorate (DiI) while simultaneously labeling sympathetic neurons with DiO, and we found a striking difference in how presynaptic axons converged onto SCG neurons (Figures 3F and 3G). In α3-KO SCG, the preganglionic axons grew extensively over the somas of sympathetic neurons (Figures 3G and 3H); the proportion of the neuron's soma covered by preganglionic axons in α3-KO SCG was at least 50% on average, likely an underestimation because the preganglionic axons were sparsely labeled in these experiments. In contrast, in WT SCG, the proportion of the soma covered by preganglionic axons was less than 5% (Figures 3F and 3H). Our ultrastructural studies support these results: comparing random sections from α3-KO and WT SCG, we detected 6 times as many varicosities bordering neuronal cell bodies in α3-KO SCG (Figures S2A and S2B). These results indicate that, in the absence of synaptic activity, preganglionic axons more readily contact the cell bodies of sympathetic neurons.

This prominent growth of preganglionic axons over SCG neuronal cell bodies in 1-month-old α3-KO mice suggests that, without synaptic activity, the axons target silent synapses onto the soma instead of preferentially onto dendrites. To determine whether this mis-targeting of synapses in α3-KO SCG is already present at birth or whether it evolves during the first post-natal month, as preganglionic innervation increases without activity, we stained varicosities of DiI-labeled axons at P1, P4, and P28 for vesicular acetylcholine transporter protein (VAChT). VAChT is highly localized in cholinergic presynaptic terminals, and over 90% of these VAChT-positive varicosities co-localized with postsynaptic density-93 (PSD-93) puncta (Krishnaswamy and Cooper, 2009; Figures S2C and S2D), suggesting that these are sites of synaptic contact.

Over the first post-natal month, the number of synapses on WT SCG neurons increased ~2-fold (Figure S2E, inset). In α3-KO mice, synapses continued to be established on SCG neurons

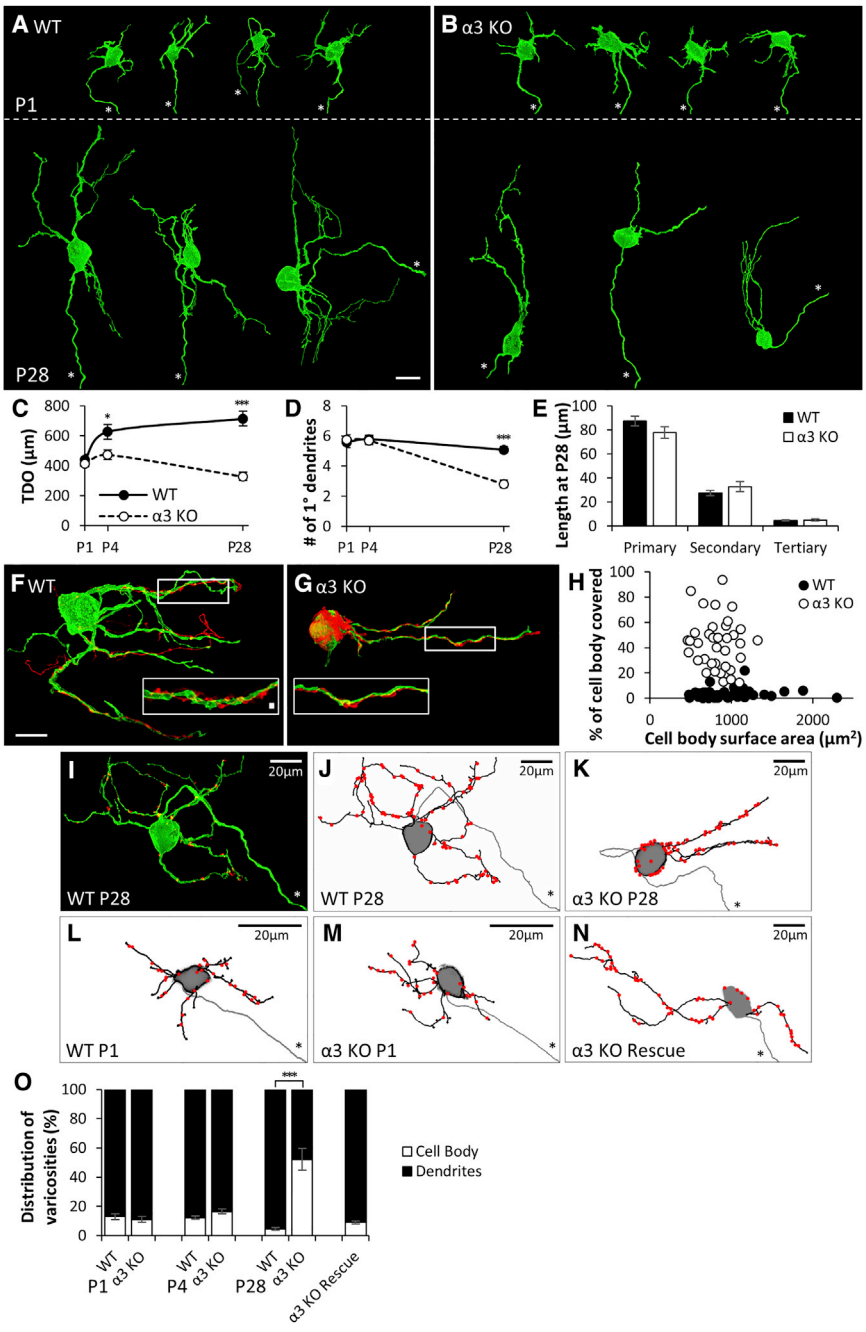

Figure 3. Primary Dendrites Are Not Maintained without Postsynaptic Activity, and Preganglionic Axons Target Silent Synapses to the Soma

(A and B) Maximum-intensity projections of DiO-labeled SCG neurons from (A) WT and (B) α3-KO mice labeled at P1 (top) and at P28 (bottom). Axons are marked by an asterisk. Scale bar, 20 μm. In each panel, neurons are from different ganglia and have been tiled for comparison.

(C) Average total dendritic outgrowth (TDO) per neuron at P1, P4, and P28; filled circles represent WT and open circles represent α3 KO in this panel and (D).

(D) Average number of primary dendrites per neuron at P1, P4, and P28.

(E) Average length of primary dendrites, secondary branches, and tertiary branches at P28; filled columns represent WT and open columns represent α3 KO.

For (C)–(E), error bars represent ± SEM. *p < 0.05 and ***p < 0.001. WT: for P1, n = 23 neurons (10 mice); for P4, n = 28 neurons (10 mice); and for P28, n = 34 neurons (12 mice). α3 KO: for P1, n = 21 neurons (10 mice); for P4, n = 24 neurons (10 mice); and for P28, n = 36 neurons (14 mice).

(F and G) Maximum-intensity projections of DiO-labeled P28 SCG neurons (green) innervated by DiI-labeled preganglionic axons (red) in (F) WT and (G) α3-KO SCG. Scale bar, 20 μm. Inset: the boxed region at higher magnification shows preganglionic axons (red) with varicosities along a segment of dendrite (green). Scale bar, 2 μm.

(H) Percentage of neuronal cell body covered by preganglionic axons for P28 SCG neurons of different sizes. (WT, filled circles, n = 50 neurons (16 mice), α3 KO, open circles, n = 38 neurons (13 mice)).

(I) DiO-labeled neuron (green) from a P28 WT SCG immunostained for VAChT (red). Axon is marked by an asterisk. VAChT puncta not touching the neurons were removed for clarity.

(J–N) Skeletonized reconstructions showing dendritic arbors (black), axon (gray, marked by an asterisk), and preganglionic axon varicosities (red), determined by VAChT staining, as in (A). (J) WT neuron from (I), (K) α3-KO neuron at P28, (L) WT neuron at P1, (M) α3-KO neuron at P1, and (N) α3-KO SCG neuron 1 month after rescue with Ad-α3 are shown. Neurons in (I)–(K) and (N) are shown at the same scale, and neurons in (L) and (M) are magnified for clarity.

(O) Average distribution of varicosities on the cell body (open) and dendrites (filled) in WT and α3-KO SCG at P1, P4, and P28 and on α3-KO neurons 1 month after rescue with Ad-α3. Error bars represent ± SEM. ***p < 0.001. WT: for P1, n = 6 neurons (3 mice); for P4, n = 9 neurons (5 mice); and for P28, n = 10 neurons (4 mice). α3 KO: for P1, n = 6 neurons (5 mice); for P4, n = 10 neurons (4 mice); and for P28, n = 11 neurons (4 mice). For α3-KO rescue, n = 12 neurons (8 mice).

during the first post-natal month, even when synaptic transmission was absent and synapses were electrophysiologically silent. When normalized to the size of the dendritic tree, the number of synapses per α3-KO neuron at P28 was ~40% greater than the number for age-matched controls (Figure S2E).

Preganglionic axons target their synapses mainly to dendrites of sympathetic neurons in WT SCG. We found that over 90% of the VAChT-positive varicosities on P1 and P4 SCG neurons were located on dendrites, and, by P28, this proportion increased to 95% (Figures 3I, 3J, 3L, and 3O). As well, in α3-KO SCG at P1–P4, synapses were mainly distributed on dendrites and not statistically different from those on age-matched WT neurons (Figures 3M and 3O). In contrast, at P28, when the preganglionic axons converged on the soma in α3-KO neurons, over 50% of

the VAChT-positive varicosities were located on the cell body (Figures 3K and 3O). Moreover, rescuing synaptic activity in the SCG of α3-KO mice at P28 (and assessed at P56) resulted in a shift in the distribution of presynaptic varicosities from the soma to the dendrites (Figures 3N and 3O), without any effect on the size of the dendritic tree. These findings indicate that synaptic activity reorganizes preganglionic synapses and targets them to dendrites of sympathetic neurons.

Levels of Phosphorylated 4E-BP Are Decreased in α3-KO SCG

Our findings demonstrate clearly that postsynaptic activity during early post-natal development is required for appropriate refinement and remodelling of synaptic connections in the SCG. Inactivity of sympathetic neurons in the SCG of α3-KO mice presumably exerts its effects by altering the synthesis of various proteins (Wells et al., 2000; Steward and Schuman, 2001; Alvarez-Castelao and Schuman, 2015). Since a growing body of evidence points to a link among regulated mRNA translation, neuronal development, and synaptic plasticity (Bramham and Wells, 2007; Jung et al., 2012), we asked whether the effects of synaptic activity on developing neural circuits in sympathetic ganglia might be mediated, at least in part, through mechanisms that regulate mRNA translation. For example, work in *Drosophila*, as well as in hippocampal neuronal primary cultures, has suggested that postsynaptic translational mechanisms can respond to changes in synaptic activity and participate in retrograde regulation of synaptic plasticity (Henry et al., 2012; Penney et al., 2012, 2016). We focused our attention on the eIF4E 4E-BPs, proteins whose phosphorylation status regulates the initiation of translation (Ma and Blenis, 2009; Sonenberg and Hinnebusch, 2007; Gingras et al., 1999; Figure 4A).

At birth, there was no significant difference in the levels of phosphorylated 4E-BP1 in α3-KO SCG neurons when compared to age-matched WT neurons (Figure 4C); however, at 1 month, phosphorylated 4E-BP1 in α3-KO SCG was ~25%–30% less than in WT SCG (Figures 4B and 4C), while total 4E-BP1 was at comparable levels (Figures 4D and 4E; Figures S3D–S3F). This finding raised the intriguing possibility that the effects of synaptic activity on developing SCG neurons are mediated, in part, by the downstream phosphorylation of 4E-BPs and the regulation of translation.

Since 4E-BP functions as a repressor of translation, one might expect that the genetic removal of 4E-BPs would enhance cap-dependent translation, independent of synaptic transmission. To test this idea, we examined SCG neurons in mice with a deletion in 4E-BP genes. SCG neurons express both 4E-BP1 and 4E-BP2 at comparable levels (Figures S3B and S3C) (in contrast to CNS neurons, which primarily express 4E-BP2); therefore, we used mice with a deletion in both genes (4E-BP1/2$^{-/-}$; referred to simply as 4E-BP KO).

In the SCG from 4E-BP-KO mice, we observed no significant difference in dendritic growth on SCG neurons during the first post-natal month compared to that on age-matched SCG neurons in WT mice (Figure S1). We also did not detect any significant difference in the targeting of preganglionic axons compared to that in the SCG of age-matched WT mice (Figure S4A). Moreover, at P1–P3, sympathetic neurons in the SCG of 4E-BP-KO mice were innervated by 7–8 axons, similar to WT SCG neurons (Figure 4F). By P8–P9, there was a mild acceleration in the elimination of preganglionic axons (average ~5 axons in WT versus average ~4 axons in 4E-BP KO); however, at P28, the preganglionic innervation of the SCG neurons in 4E-BP mutant mice was indistinguishable from that of WT SCG neurons (Figure 4F).

SCG Proteomic Profile Is Significantly Changed in the Absence of Synaptic Activity and Largely Restored by the Removal of 4E-BP

Next, we conducted a proteomic profiling of SCG from 1-month-old WT, α3-KO, and 4E-BP-KO mice. In addition, we investigated whether removing 4E-BP influences the profile of SCG when synaptic transmission is absent. Therefore, we crossed 4E-BP KO with α3 KO to generate α3/4E-BP-double-knockout (DKO) mutant mice; the SCG in these mice had no 4E-BP or synaptic transmission (Figures 4G and 4H).

Using a data-independent acquisition SWATH workflow (Gillet et al., 2012), we quantified over 2,100 proteins expressed in the SCG, including representatives from all the major molecular function and protein classes (Figure S5; see the Experimental Procedures). Between α3-KO and WT SCG, at least 83 proteins were expressed at significantly different levels (greater than ±1.25-fold change at a q-value < 0.05); several of these are involved in mitochondrial function. Figure 5A shows a heatmap for these 83 proteins (*Z* score ratios), and it indicates that loss of synaptic activity led to significant changes in the SCG proteome. To determine the impact of removing 4E-BP on translation in the SCG when synaptic activity is absent, we examined the proteome of α3/4E-BP-DKO SCG. Of the 83 proteins whose levels were altered in α3-KO SCG, over 60% (51/83) were reversed and closer to levels in WT SCG (Figure 5A; Table S3). On the other hand, a similar comparison between WT and 4E-BP-KO SCG revealed insignificant differences for >99% of all proteins between the two groups, suggesting that, when fast synaptic transmission was intact, loss of 4E-BP had little effect on the proteome in the SCG.

Loss of 4E-BP Restores Synaptic Refinement and Remodelling in the Absence of Activity

Since removing 4E-BP from α3-KO SCG restores the majority of proteins toward their WT levels, we examined whether it also restores the synaptic organization in the SCG of α3/4E-BP-DKO mice. At P28, total dendritic outgrowth on SCG neurons in α3/4E-BP-DKO mice was approximately twice that of age-matched α3-KO neurons and about 90% of WT neurons (Figures 5B and 5C). Also, α3/4E-BP-DKO SCG neurons at 1 month maintained 5 primary dendrites, in contrast to 3 primary dendrites maintained on age-matched neurons in the SCG in α3-KO mice (Figure 5D). These results show that the genetic removal of 4E-BP largely restores normal dendritic growth, even though the SCG had no synaptic transmission.

In addition, the removal of 4E-BP from α3-KO mice influenced the targeting of synapses by preganglionic axons. At the end of the first post-natal month, the distribution of

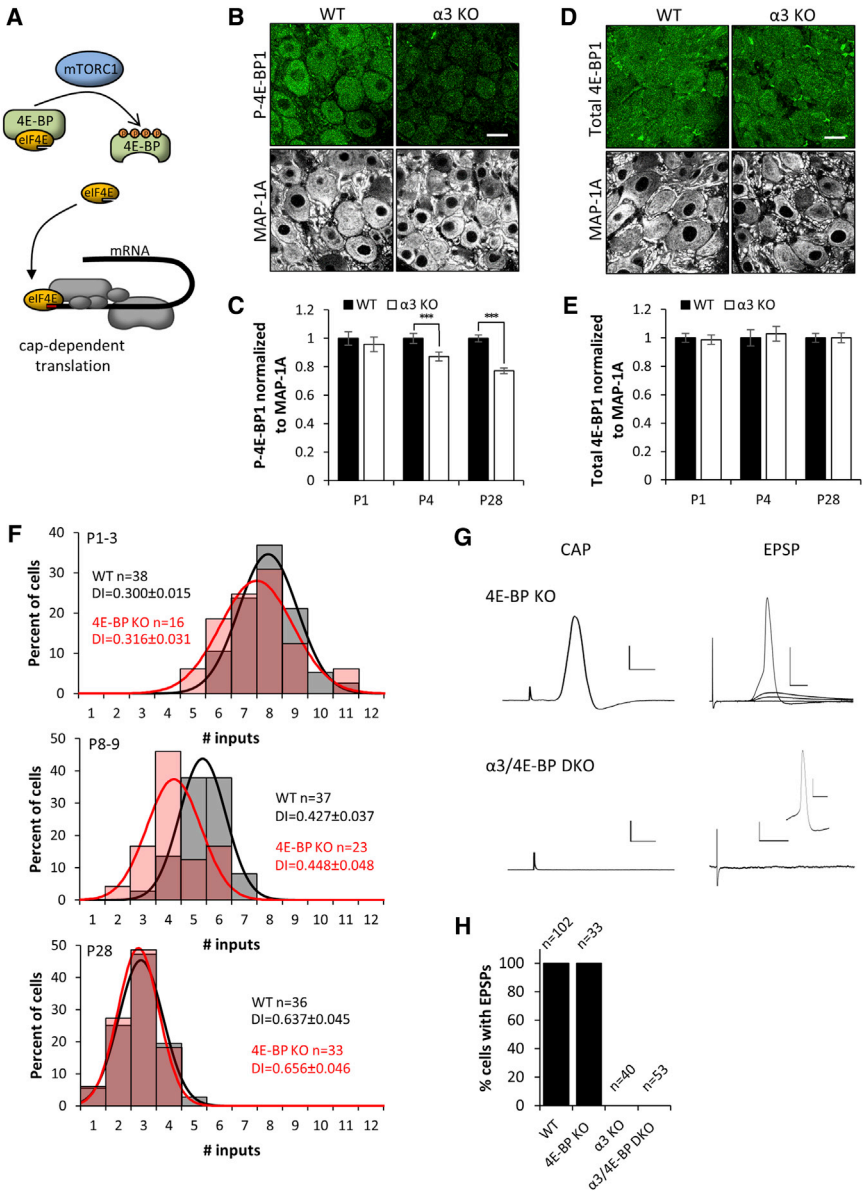

Figure 4. Levels of Phosphorylated 4E-BP Are Higher in WT SCG Than in α3-KO SCG

(A) Illustration showing cap-dependent translation, governed by the availability of eIF4E, which is regulated by 4E-BP, a major downstream target of the mTORC1 complex. Hypophosphorylated 4E-BP represses the initiation of cap-dependent translation by sequestering eIF4E. When hyperphosphorylated, 4E-BP releases eIF4E, which interacts with eIF4G and other initiation factors to initiate cap-dependent translation.

(B) Confocal images showing immunostaining for P-4E-BP1 (green) and MAP-1A (white) in WT and α3-KO SCG at P28. Scale bar, 20 μm.

(C) P-4E-BP1 mean fluorescence intensity per neuron normalized to MAP-1A in WT and α3-KO neurons at P1, P4, and P28. Filled columns represent WT and open columns represent α3 KO.

(D) Confocal images showing immunostaining for total 4E-BP1 (green) and MAP-1A (white) in WT and α3-KO SCG at P28. Scale bar, 20 μm.

(E) Total 4E-BP1 mean fluorescence intensity per neuron normalized to MAP-1A in WT and α3-KO neurons at P1, P4, and P28. Filled columns represent WT and open columns represent α3 KO. For (C) and (E), error bars represent ± SEM. ***$p < 0.001$. For WT in (C) and (E), n = 90 neurons (4 mice) for P1, n = 90 neurons (4 mice) for P4, n = 300 neurons (4 mice) for P28; and for α3 KO, n = 90 neurons (4 mice) for P1, n = 90 neurons (4 mice) for P4, and n = 300 neurons (4 mice) for P28.

(F) Distribution of SCG neurons innervated by the number of inputs in WT (gray) and 4E-BP-KO (red) mice at P1–P3, P8–P9, and P28. Each distribution is fit with a Gaussian function. The distributions at P1–P3 and at P28 are not significantly different ($p > 0.2$), whereas at P8–P9, $p < 0.05$. Each distribution contains data from at least 4 mice. n, number of neurons; DI, disparity index. Data for WT P1–P3 and P28 are from Figures 1A and 1B.

(G) Left: extracellular recordings from the SCG postganglionic nerve at P28 in response to supramaximal stimulation of the preganglionic axons. Compound action potentials were evoked in 4E-BP-KO SCG, but not in α3/4E-BP-DKO SCG. Right: intracellular recordings from an SCG neuron in response to stimulation of the preganglionic axons. EPSPs and action potentials were recorded in SCG neurons from P28 4E-BP-KO mice, but not detected in SCG neurons from α3/4E-BP-DKO mice; inset shows that SCG neurons are capable of firing action potentials. Scale bars represent 1 mV and 5 ms for the CAP and 20 mV and 10 ms for the EPSPs on 4E-BP-KO neurons and 2 mV and 20 ms on α3/4E-BP DKO. The inset is 20 mV and 10 ms.

(H) Graph shows percentage of SCG neurons that had EPSPs in response to supramaximal stimulation of the preganglionic nerve. WT (8 mice); 4E-BP KO (6 mice); α3 KO (4 mice); and α3/4E-BP DKO (8 mice). n, number of neurons. These results demonstrate that there is no synaptic transmission in α3-KO or α3/4E-BP-DKO SCG.

synapses on sympathetic neurons in the SCG of α3/4E-BP-DKO mice was similar to that on WT neurons, and it was significantly different from that on α3-KO SCG. Over 95% of synapses on the SCG neurons in α3/4E-BP-DKO mice were located on dendrites, in contrast to that on α3-KO SCG, where over 50% were located to the soma (Figures 5E and 5F; Figure S4A). These results show that genetic removal of 4E-BP largely restores dendritic targeting of presynaptic innervation on SCG neurons that are synaptically silent during development.

Since removing 4E-BP from α3-KO neurons restored the targeting of synapses to dendrites and increased dendritic growth, we wondered whether synaptic refinement would be restored in double-mutant mice even in the absence of postsynaptic activity. To address this possibility, we compared the number of preganglionic inputs that converged onto SCG neurons in α3/4E-BP-DKO mice at P28 to the number that converged onto SCG neurons in α3-KO mice.

Remarkably, SCG neurons in 1-month-old α3/4E-BP-DKO mice were innervated by only ~3 preganglionic axons,

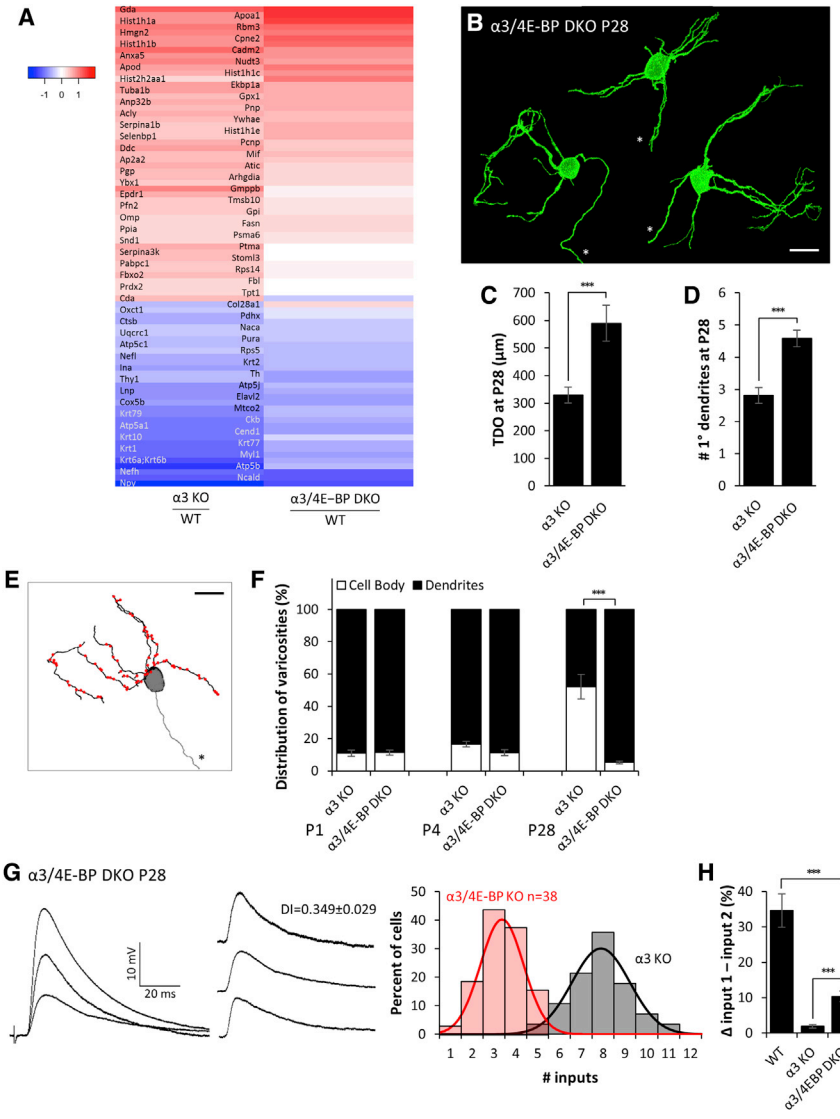

Figure 5. Genetic Removal of 4E-BP Bypasses the Need for Synaptic Activity and Restores Dendritic Morphology, Synaptic Targeting, and Refinement of Inputs in α3/4E-BP-DKO Mice

(A) Heatmap showing the $\log_2$ *Z* score ratios of protein levels for 83 proteins whose levels were significantly different (±1.25x, q-value < 0.05) between α3-KO and WT SCG. Many of the differences were restored in α3/4E-BP DKO. All mice were P28. See Figure S5 and Table S3.

(B) Maximum-intensity projections of DiO-labeled P28 SCG neurons from α3/4E-BP-DKO mice. All neurons are shown at the same scale; axons are marked by an asterisk. Scale bar, 20 μm. Neurons are from different ganglia and have been tiled for comparison.

(C) Average total dendritic outgrowth (TDO) per neuron at P28 in α3-KO (from Figure 3C) and α3/4E-BP-DKO SCG.

(D) Average number of primary dendrites per neuron at P28 in α3-KO (from Figure 3D) and α3/4E-BP-DKO SCG.

(E) Skeletonized reconstruction of a P28 neuron in α3/4E-BP-DKO SCG showing dendritic arbors (black), axon (gray, marked by an asterisk), and the locations of preganglionic axon varicosities (red), determined by VAChT staining. Scale bar, 20 μm.

(F) Average distribution of varicosities on the cell body (open) and dendrites (filled) in α3-KO (from Figure 3O) and α3/4E-BP-DKO SCG at P1, P4, and P28.

For (C), (D), and (F), error bars represent ± SEM. ***p < 0.001. For (C) and (D), α3/4E-BP DKO: n = 24 neurons (10 mice). For (F), α3/4E-BP DKO: at P1 n = 6 neurons (3 mice); at P4, n = 7 neurons (4 mice); and at P28, n = 10 neurons (4 mice).

(G) Left: EPSPs evoked on a P28 SCG neuron from α3/4E-BP-DKO mice. Middle: EPSPs evoked by individual preganglionic axons. DI, disparity index. Right: distribution of P28 SCG neurons in α3/4E-BP-DKO (red) and α3-KO (gray; from Figure 1D) mice innervated by the number of inputs. The distribution is fit with a Gaussian function.

(H) The average difference in strength between the strongest and second strongest inputs, expressed as a percentage of the maximum compound EPSP in WT, α3-KO, and α3/4E-BP-DKO SCG. Error bars represent ± SEM. ***p < 0.001.

significantly fewer than the 7–8 on age-matched α3-KO neurons (Figure 5G), but not statistically different from the 2–3 axons innervating SCG neurons in 4E-BP-KO or WT mice. These results indicate that removal of 4E-BP from α3-KO mice restores the ability of preganglionic axons to refine, even though synaptic transmission is absent and synapses remain silent.

The persistent preganglionic inputs to SCG neurons in α3/4E-BP-DKO mice increased in strength, but unlike WT SCG, the disparity among these inputs was small, but greater than that in α3 KO; this is reflected both by the disparity index (Figure 5G) and by the difference in strength between the strongest input and second strongest input (Figure 5H). These results suggest that activity-dependent mechanisms controlling axon elimination are distinct from those that control the differential strengthening of refined connections.

DISCUSSION

During the first post-natal month, connections between preganglionic inputs and postsynaptic sympathetic neurons in the mouse SCG undergo a robust refinement and dendritic remodeling. In this study, we demonstrate that this developmental reorganization is mediated by synaptic activity and that when synaptic activity is absent, regulating cap-dependent translation influences the re-organization of synaptic connections. Our work shows that in mice lacking fast nicotinic transmission in SCG because of a deletion in the α3 nAChR subunit gene (α3 KO), the reorganization of synaptic connections is severely disrupted: the targeting of synapses on postsynaptic neurons is impaired, and preganglionic axons fail to refine. Virally re-introducing the missing α3 and re-establishing synaptic transmission

restores these features to those in WT SCG. These results clearly establish that synaptic activity is both necessary and sufficient for the reorganization and refinement of synaptic connections in the mouse SCG. A key finding of our study is that enhancing cap-dependent translation by genetic removal of the translational repressor 4E-BP leads to a remarkable recovery in the reorganization of connections, and synapse elimination occurred even though fast synaptic transmission was absent; this demonstrates a remarkable degree of plasticity by silent synapses. Sympathetic neurons in mice homozygous for mutations in both α3 and 4E-BP (α3/4E-BP-DKO) closely resemble those in WT type mice in terms of the number of presynaptic inputs, dendritic growth, and synaptic distribution. Our results indicate that when postsynaptic activity is absent, considerable reorganization of synaptic connections can still take place by enhancing cap-dependent translation.

Synaptic refinement is a competitive process in which converging axons of similar type compete with one another to innervate a target. As development proceeds, the synaptic strength of 1 or more axons increases; it is thought that this differential in synaptic strength among competing axons gives the stronger inputs an advantage for consolidation, while weaker inputs are eliminated (Lichtman and Colman, 2000; Busetto et al., 2000; Bosman et al., 2008; Turney and Lichtman, 2012; Lee et al., 2014; but see Wang et al. 2011). In the SCG of α3/4E-BP-DKO mice, there is less differential strengthening among inputs; nonetheless, synapse elimination of preganglionic axons occurs in the absence of synaptic transmission. Therefore, in sympathetic ganglia, a differential in synaptic strength does not determine which axons are retained and/or which are eliminated, challenging the notion that a differential in synaptic strength determines which synapses are stabilized and which are eliminated (Katz and Shatz, 1996; Piochon et al., 2016).

The Effects of Activity and Removing 4E-BP on Protein Levels

Our proteomic experiments demonstrate that a significant number of proteins are altered when postsynaptic activity is absent and the loss of 4E-BP in α3-KO mutant mice largely restores the proteome. In its basal state, hypo-phosphorylated 4E-BP suppresses cap-dependent translation by sequestering eIF4E and preventing the formation of the 5′ cap. Several signals initiate cap-dependent translation, directly or indirectly, by hyperphosphorylating 4E-BP and releasing eIF4E. We show that, in SCG neurons, fast excitatory synaptic transmission is one such signal that leads to increased 4E-BP phosphorylation and, by extension, cap-dependent translation. Similarly, deletion of 4E-BP removes this sequestration of eIF4E, leading to enhanced cap-dependent translation and altered protein levels. How organisms tolerate genetic alteration of major regulators of cap-dependent translation, such as loss of 4E-BP or heterozygocity for eIF4E, is the subject of intense experimental investigations. Recent discoveries suggest that specific mRNAs and, therefore, specific pathways rather than overall maintenance of proteins are affected as a result of these manipulations (Truitt et al., 2015; Gkogkas et al. 2013).

Consistent with this notion, we found that loss of 4E-BP had little effect on the development and innervation of SCG neurons or on the global proteome profile of SCG; of the 2,100 specific proteins identified at the SCG, only a few showed differential expression as a result of the loss of 4E-BP. By contrast, the absence of excitatory synaptic transmission had a significant effect on the global proteome profile: we found that the levels of at least 83 proteins were significantly altered in α3-KO SCG, indicating that these proteins are regulated by pathways downstream of postsynaptic activity and possibly involved in the refinement of presynaptic inputs, the stability of primary dendritic branches, and the targeting of synapses by preganglionic axons. Relevantly, deleting 4E-BP from α3-KO mice changed the proteomic profile of SCG and shifted the levels of more than half of these proteins toward values found in WT SCG.

Interestingly, the levels of a large number of proteins were not statistically different between WT and α3-KO SCG, suggesting that these proteins are not directly regulated by postsynaptic activity. Of particular interest are proteins implicated in synapse elimination elsewhere in the nervous system. For example, the major histocompatibility complex class 1 molecules H2-D^b and H2-K^b are involved in refinement of retinal ganglion cell axons innervating the lateral geniculate nucleus (LGN) through a mechanism that regulates the expression of postsynaptic AMPA receptors (Lee et al., 2014). We found no difference in the levels of major histocompatibility complex class 1 molecule H2-D^b between α3-KO and WT SCG, and we did not detect H2-K^b. Moreover, we detected no statistical difference in the level of the complement proteins C1q and C3, molecules required for the elimination of retinal ganglion cell synapses in the LGN (Stevens et al., 2007; Stephan et al., 2012). These results suggest that other molecules and pathways are involved in synapse elimination in the SCG.

Our proteomic analysis provides a comprehensive profile of activity-dependent protein expression in mouse SCG, not only revealing that postsynaptic activity during the first post-natal month has a profound effect on the proteomic landscape in the SCG but also confirming that the removal of 4E-BP can largely normalize the proteomic landscape in the absence of activity. These experiments pave the way for future work aimed at identifying a mechanistic link between individual or a network of multiple proteins and the developmental program of refinement at the SCG.

Distribution of Silent Synapses

As axons are being eliminated in WT SCG during the first post-natal month, those that persist strengthen their inputs by increasing the number of synaptic contacts on sympathetic neurons, and, by the first post-natal month, the overall number of synapses on SCG neurons is ~2-fold greater than at birth. Although the increase in synapses overlaps in time with axon elimination, our results from α3-KO SCG suggest that these two processes are regulated by different mechanisms. Synaptic contacts in α3-KO SCG continue to increase over the first post-natal month in an activity-independent manner, whereas synapse elimination depends critically on activity. Moreover, in α3-KO adult SCG, the density of synaptic contacts on sympathetic neurons is approximately 40% greater than that

on neurons in WT SCG, even though axon elimination does not occur. This indicates that the increase in synapses and the elimination of axons are likely regulated by different mechanisms.

Postsynaptic activity plays a crucial role in determining how preganglionic axons target their synapses onto sympathetic neurons during post-natal development. At birth, most synapses are targeted to dendrites in both WT and α3-KO SCG. Yet, over the first post-natal month, as synapses are continually formed, the preganglionic axons in WT SCG continue to target their synapses to dendrites, while most synapses in α3-KO SCG at 1 month are targeted to and hyperinnervate the soma of these synaptically inactive neurons, as if, in the absence of activity, sympathetic neurons actively seek innervation. Furthermore, restoring postsynaptic activity to α3-KO SCG neurons results in a shift in distribution of synapses from the soma to the dendrites, indicating that the targeting of synapses to the dendrites of sympathetic neurons remains plastic and the distribution of synapses is directed by mechanisms downstream of postsynaptic activity. Notably, when 4E-BP is deleted from α3-KO mice, electrophysiologically silent synaptic contacts continue to increase in the first post-natal month at a density similar to WT. These results suggest that, upon the removal of 4E-BP, the preganglionic axons target their synapses to dendrites, bypassing the normal requirement for postsynaptic activity.

Dendritic Growth

Dendrites on neurons in α3-KO SCG grow poorly over the first post-natal month. This is consistent with several studies demonstrating that disrupting synaptic activity influences the growth of dendrites (Wong and Ghosh, 2002; Cline and Haas, 2008; Lefebvre et al., 2015). However, our findings are at odds with previous work showing that cutting the preganglionic nerve at birth had no effect on the growth of dendrites on denervated neurons over the first post-natal month (Voyvodic, 1987). It is not clear why inactivity produced by the deletion of α3 has a different effect on dendritic growth by SCG neurons than inactivity produced by cutting the preganglionic nerve. It seems unlikely that α3 has some unanticipated role in dendritic growth and stabilization, apart from its role in forming functional nAChRs and mediating fast synaptic transmission, because, when placed in culture, α3-KO and WT SCG neurons extend dendrites that are statistically similar (Figures S1J and S1K).

Neurons in the SCG receive cholinergic-nicotinic synaptic transmission before birth (Rubin, 1985), raising the possibility that a reduction in synaptic activity in α3-KO SCG in utero might have influenced the growth of dendrites. However, this seems unlikely because: (1) the activity is low in the sympathetic nervous system prenatally, as the mother maintains the pups' homeostasis in utero; and (2) at birth, dendrites on α3-KO SCG are not statistically different from control WT neurons.

A clear distinction between α3-KO neurons and denervated neurons is that α3-KO neurons receive morphological synapses. Conceivably, the difference in dendritic growth between α3-KO SCG neurons and denervated WT neurons is that α3-KO SCG neurons have electrophysiologically silent synapses. If the silent synapses signal inappropriately to molecules downstream of the postsynaptic complex to perturb dendritic growth (Quach et al., 2013), it might account for the difference between dendritic growth on inactive α3-KO SCG neurons and those on denervated neurons. Whatever the molecules involved, we show that 4E-BP-regulated translation can act on such pathways to control dendritic growth.

In summary, our findings demonstrate that 4E-BP-regulated mechanisms are involved in the growth of dendrites, the targeting of synapses, and the refinement of preganglionic axons when postsynaptic activity is absent. Our findings suggest that, in the absence of synaptic activity, where synaptic refinement is curtailed, genetic removal of 4E-BP activates a molecular program that can compensate for the lack of activity-dependent mechanisms that normally direct synaptic reorganization and refinement of presynaptic inputs.

EXPERIMENTAL PROCEDURES

Experimental Model and Subject Details

Mice

Mice with a deletion in the alpha 3 nicotinic subunit gene (Xu et al., 1999; referred to as α3 KO) were maintained on an outcrossed background (Krishnaswamy and Cooper, 2009). To generate 4EBP1/2$^{-/-}$; α3$^{-/-}$ mice (referred to as α3/4E-BP DKO) a series of crosses were performed between 4EBP1/2$^{-/-}$ mice (Tsukiyama-Kohara et al., 2001; Banko et al., 2005) and α3 KO mice. Genotypes for all three genes were determined by PCR (Figure S3A). Our results include data from both male and female mice. All procedures for animal handling were carried out according to the guidelines of the Canadian Council on Animal Care.

Method Details

Electrophysiological Recordings

For intracellular recordings, we used 80–120 mΩ glass microelectrodes attached to a high inertial precision microdrive. The recording electrode was filled with 1M KAc and connected to the head stage of an Axoclamp 2A amplifier used in current-clamp mode. On-line stimulation and data acquisition were done with N-Clamp and offline data analysis was performed using Igor Pro software. To measure dendrites on Ad-α3 infected neurons, electrodes were filled with 10mM Alexa Fluor 488 hydrazide in 200mM KCl.

To measure the convergence of preganglionic axons innervating a sympathetic neuron, the preganglionic nerve was stimulated with voltages of increasing strength while holding the neuron at ~-90 mV to prevent EPSPs from triggering action potentials. In some experiments, we also included QX314 in the recording electrode to prevent action potentials. Increasing the strength of the stimulus to the preganglionic nerve activates axons of different thresholds which results in discrete jumps in the amplitude of the EPSPs. We used these discrete jumps as a measure of the number of axons innervating the neuron. To isolate the EPSP evoked by individual axons, we averaged at least 10 traces for each discrete jump and calculated the difference between the average EPSP evoked by that axon and all axons of lower threshold and the average EPSP evoked only by axons of lower threshold. To calculate the disparity index, DI, for each neuron, we divided the standard deviation, SD, of the EPSPs by the mean EPSP (Hashimoto and Kano, 2003).

Adenoviruses

Full-length α3 neuronal nAChR subunit cDNA was ligated with either the synapsin or human ubiquitin C promoter into pAdTrack (Ad-α3/Syn or Ad-α3/Ubi) and infected mice with either Ad-α3/Syn or Ad-α3/Ubi adenovirus at a concentration of ~10^7 pfu/mL.

Lipophilic Tracer Labeling

We used lipophilic tracers DiI and DiO to sparsely label a random subset of preganglionic axons and postsynaptic neurons in the SCG. After labeling, ganglia were kept in the dark in 1X PBS for 5 - 6 days to allow for tracers to diffuse along the axons. Ganglia were sliced into 100 μm sections.

Immunohistochemistry

Details are described in Supplemental Experimental Procedures.

Image Acquisition and Analysis

Images were acquired on an upright confocal microscope (BX-61W, Olympus) with a 60X, NA 1.42 PlanApo N oil-immersion objective. Laser lines were activated sequentially. All analysis was performed with ImageJ (NIH, Bethesda, MD).

Dendrite analysis. Only neurons with complete dendritic arbors and an identifiable axon were analyzed. For images of isolated neurons, we removed all DiO-labeled neurites that were not connected to the neuron of interest, as determined from 3D reconstructions. To quantify the length and number of dendritic branches, we reconstructed neurons in 3D.

Synaptic targeting. For synaptic targeting, we identified VAChT puncta located on a neuron of interest on each plane of a z stack. VAChT puncta that co-localized with the DiO membrane label, were at least 0.5 μm in diameter, and spanned at least two optical slices were counted as putative synapses.

Preganglionic axonal targeting. To estimate the percentage of the cell body surface covered by an axon, on each plane of the cell body, we measured the circumference of the cell body (DiO labeled from postganglionic nerve), and the proportion of the cell body circumference occupied by an axon (DiI labeled from preganglionic nerve) on that plane.

P-4E-BP1, 4E-BP1 and MAP-1A fluorescence intensity. For intensity analysis, average fluorescence intensity for each ROI was measured from the MAP-1A channel, and ROI were transferred to the P-4E-BP1 or 4E-BP1 channel to measure the corresponding fluorescence intensity.

Proteomics

Full details for the proteomic experiments are in the Supplemental Experimental Procedures.

Quantification and Statistical Analysis

Values of n and p values are reported in the Figures and corresponding figure legends. In all figures, error bars represent ± SEM, *$p < 0.05$, ***$p < 0.001$. To test for statistical differences between two samples, we used unpaired two-tailed t tests assuming equal variance; for three or more samples, we used a one-way ANOVA to determine if one or more samples were significantly different. If the p value calculated from the F-statistic was less than 0.05, we used a post hoc Tukey HSD test to identify which pairs of samples were significantly different from each other.

DATA AND SOFTWARE AVAILABILITY

The accession numbers for the raw proteomics reported in this paper are ProteomeXchange: PXD007141 and MassIVE: MSV000081386, and can also be accessed at ftp://massive.ucsd.edu/MSV000081386.

SUPPLEMENTAL INFORMATION

Supplemental Information includes Supplemental Experimental Procedures, five figures, and three tables and can be found with this article online at https://doi.org/10.1016/j.celrep.2018.03.040.

ACKNOWLEDGMENTS

This work was supported by Canadian Institute for Health Research operating grants to A.P.H., N. Sonenberg, and E.C. We thank Professor L. Cooper for comments on the manuscript. The proteomics analysis was partially funded by an NIH shared instrumentation grant for the TripleTOF system at the Buck Institute (1S10 OD016281). N.B. received a fellowship from the Glenn Foundation for Medical Research.

AUTHOR CONTRIBUTIONS

Conceptualization, Y.C., E.C., and A.P.H.; Methodology, Y.C., N. Saviuk, B.P., N. Sonenberg, E.C., B.S., and A.P.H.; Investigation, Y.C., B.P., E.C., N. Saviuk, A.P.H., N.B., R.K.Q., and B.S.; Writing – Original Draft, Y.C. and E.C.; Writing – Review & Editing, Y.C., N. Saviuk, B.P., N. Sonenberg, E.C., A.P.H., N.B., and B.S.; Visualization, Y.C., E.C., and A.P.H.; Funding Acquisition, E.C. and A.P.H.

DECLARATION OF INTERESTS

The authors declare no competing interests.

Received: October 20, 2016
Revised: February 2, 2018
Accepted: March 10, 2018
Published: April 3, 2018

REFERENCES

Alvarez-Castelao, B., and Schuman, E.M. (2015). The Regulation of Synaptic Protein Turnover. J. Biol. Chem. *290*, 28623–28630.

Balice-Gordon, R.J., and Lichtman, J.W. (1994). Long-term synapse loss induced by focal blockade of postsynaptic receptors. Nature *372*, 519–524.

Banko, J.L., Poulin, F., Hou, L., DeMaria, C.T., Sonenberg, N., and Klann, E. (2005). The translation repressor 4E-BP2 is critical for eIF4F complex formation, synaptic plasticity, and memory in the hippocampus. J. Neurosci. *25*, 9581–9590.

Bleckert, A., and Wong, R.O.L. (2011). Identifying roles for neurotransmission in circuit assembly: insights gained from multiple model systems and experimental approaches. BioEssays *33*, 61–72.

Bosman, L.W., Takechi, H., Hartmann, J., Eilers, J., and Konnerth, A. (2008). Homosynaptic long-term synaptic potentiation of the "winner" climbing fiber synapse in developing Purkinje cells. J. Neurosci. *28*, 798–807.

Bramham, C.R., and Wells, D.G. (2007). Dendritic mRNA: transport, translation and function. Nat. Rev. Neurosci. *8*, 776–789.

Buffelli, M., Busetto, G., Cangiano, L., and Cangiano, A. (2002). Perinatal switch from synchronous to asynchronous activity of motoneurons: link with synapse elimination. Proc. Natl. Acad. Sci. USA *99*, 13200–13205.

Busetto, G., Buffelli, M., Tognana, E., Bellico, F., and Cangiano, A. (2000). Hebbian mechanisms revealed by electrical stimulation at developing rat neuromuscular junctions. J. Neurosci. *20*, 685–695.

Cline, H.T. (2001). Dendritic arbor development and synaptogenesis. Curr. Opin. Neurobiol. *11*, 118–126.

Cline, H., and Haas, K. (2008). The regulation of dendritic arbor development and plasticity by glutamatergic synaptic input: a review of the synaptotrophic hypothesis. J. Physiol. *586*, 1509–1517.

Cohen-Cory, S. (2002). The developing synapse: construction and modulation of synaptic structures and circuits. Science *298*, 770–776.

Fitzsimonds, R.M., and Poo, M.M. (1998). Retrograde signaling in the development and modification of synapses. Physiol. Rev. *78*, 143–170.

Forehand, C.J. (1985). Density of somatic innervation on mammalian autonomic ganglion cells is inversely related to dendritic complexity and preganglionic convergence. J. Neurosci. *5*, 3403–3408.

Gillet, L.C., Navarro, P., Tate, S., Rost, H., Selevsek, N., Reiter, L., Bonner, R., and Aebersold, R. (2012). Targeted data extraction of the MS/MS spectra generated by data-independent acquisition: a new concept for consistent and accurate proteome analysis. Mol. Cell Proteomics. *11*, O111.016717.

Gingras, A.-C., Gygi, S.P., Raught, B., Polakiewicz, R.D., Abraham, R.T., Hoekstra, M.F., Aebersold, R., and Sonenberg, N. (1999). Regulation of 4E-BP1 phosphorylation: a novel two-step mechanism. Genes Dev. *13*, 1422–1437.

Gkogkas, C.G., Khoutorsky, A., Ran, I., Rampakakis, E., Nevarko, T., Weatherill, D.B., Vasuta, C., Yee, S., Truitt, M., Dallaire, P., et al. (2013). Autism-related deficits via dysregulated eIF4E-dependent translational control. Nature *493*, 371–377.

Haas, K., Li, J., and Cline, H.T. (2006). AMPA receptors regulate experience-dependent dendritic arbor growth in vivo. Proc. Natl. Acad. Sci. USA *103*, 12127–12131.

Hashimoto, K., and Kano, M. (2003). Functional differentiation of multiple climbing fiber inputs during synapse elimination in the developing cerebellum. Neuron *38*, 785–796.

Hashimoto, K., Tsujita, M., Miyazaki, T., Kitamura, K., Yamazaki, M., Shin, H.-S., Watanabe, M., Sakimura, K., and Kano, M. (2011). Postsynaptic P/Q-type Ca2+ channel in Purkinje cell mediates synaptic competition and elimination in developing cerebellum. Proc. Natl. Acad. Sci. USA *108*, 9987–9992.

Hata, Y., and Stryker, M.P. (1994). Control of thalamocortical afferent rearrangement by postsynaptic activity in developing visual cortex. Science *265*, 1732–1735.

Henry, F.E., McCartney, A.J., Neely, R., Perez, A.S., Carruthers, C.J., Stuenkel, E.L., Inoki, K., and Sutton, M.A. (2012). Retrograde changes in presynaptic function driven by dendritic mTORC1. J. Neurosci. *32*, 17128–17142.

Hong, Y.K., and Chen, C. (2011). Wiring and rewiring of the retinogeniculate synapse. Curr. Opin. Neurobiol. *21*, 228–237.

Jung, H., Yoon, B.C., and Holt, C.E. (2012). Axonal mRNA localization and local protein synthesis in nervous system assembly, maintenance and repair. Nat. Rev. Neurosci. *13*, 308–324.

Kano, M., and Hashimoto, K. (2009). Synapse elimination in the central nervous system. Curr. Opin. Neurobiol. *19*, 154–161.

Katz, L.C., and Crowley, J.C. (2002). Development of cortical circuits: lessons from ocular dominance columns. Nat. Rev. Neurosci. *3*, 34–42.

Katz, L.C., and Shatz, C.J. (1996). Synaptic activity and the construction of cortical circuits. Science *274*, 1133–1138.

Krishnaswamy, A., and Cooper, E. (2009). An activity-dependent retrograde signal induces the expression of the high-affinity choline transporter in cholinergic neurons. Neuron *61*, 272–286.

Lee, H., Brott, B.K., Kirkby, L.A., Adelson, J.D., Cheng, S., Feller, M.B., Datwani, A., and Shatz, C.J. (2014). Synapse elimination and learning rules co-regulated by MHC class I H2-Db. Nature *509*, 195–200.

Lefebvre, J.L., Sanes, J.R., and Kay, J.N. (2015). Development of dendritic form and function. Annu. Rev. Cell Dev. Biol. *31*, 741–777.

Lichtman, J.W., and Colman, H. (2000). Synapse elimination and indelible memory. Neuron *25*, 269–278.

Lin, T.V., Hsieh, L., Kimura, T., Malone, T.J., and Bordey, A. (2016). Normalizing translation through 4E-BP prevents mTOR-driven cortical mislamination and ameliorates aberrant neuron integration. Proc. Natl. Acad. Sci. USA *113*, 11330–11335.

Ma, X.M., and Blenis, J. (2009). Molecular mechanisms of mTOR-mediated translational control. Nat. Rev. Mol. Cell Biol. *10*, 307–318.

Niell, C.M., Meyer, M.P., and Smith, S.J. (2004). In vivo imaging of synapse formation on a growing dendritic arbor. Nat. Neurosci. *7*, 254–260.

Penney, J., Tsurudome, K., Liao, E.H., Elazzouzi, F., Livingstone, M., Gonzalez, M., Sonenberg, N., and Haghighi, A.P. (2012). TOR is required for the retrograde regulation of synaptic homeostasis at the Drosophila neuromuscular junction. Neuron *74*, 166–178.

Penney, J., Tsurudome, K., Liao, E.H., Kauwe, G., Gray, L., Yanagiya, A., R Calderon, M., Sonenberg, N., and Haghighi, A.P. (2016). LRRK2 regulates retrograde synaptic compensation at the Drosophila neuromuscular junction. Nat. Commun. *7*, 12188.

Piochon, C., Kano, M., and Hansel, C. (2016). LTD-like molecular pathways in developmental synaptic pruning. Nat. Neurosci. *19*, 1299–1310.

Purves, D., and Lichtman, J.W. (1980). Elimination of synapses in the developing nervous system. Science *210*, 153–157.

Purves, D., and Lichtman, J. (1984). Principles of Neural Development (Massachusetts: Sinauer Associates Inc.).

Quach, D.H., Oliveira-Fernandes, M., Gruner, K.A., and Tourtellotte, W.G. (2013). A sympathetic neuron autonomous role for Egr3-mediated gene regulation in dendrite morphogenesis and target tissue innervation. J. Neurosci. *33*, 4570–4583.

Rassadi, S., Krishnaswamy, A., Pié, B., McConnell, R., Jacob, M.H., and Cooper, E. (2005). A null mutation for the alpha3 nicotinic acetylcholine (ACh) receptor gene abolishes fast synaptic activity in sympathetic ganglia and reveals that ACh output from developing preganglionic terminals is regulated in an activity-dependent retrograde manner. J. Neurosci. *25*, 8555–8566.

Richter, J.D., and Sonenberg, N. (2005). Regulation of cap-dependent translation by eIF4E inhibitory proteins. Nature *433*, 477–480.

Rubin, E. (1985). Development of the rat superior cervical ganglion: initial stages of synapse formation. J. Neurosci. *5*, 697–704.

Sanes, J.R., and Lichtman, J.W. (1999). Development of the vertebrate neuromuscular junction. Annu. Rev. Neurosci. *22*, 389–442.

Schlaggar, B.L., Fox, K., and O'Leary, D.D. (1993). Postsynaptic control of plasticity in developing somatosensory cortex. Nature *364*, 623–626.

Sonenberg, N., and Hinnebusch, A.G. (2007). New modes of translational control in development, behavior, and disease. Mol. Cell *28*, 721–729.

Sonenberg, N., and Hinnebusch, A.G. (2009). Regulation of translation initiation in eukaryotes: mechanisms and biological targets. Cell *136*, 731–745.

Stephan, A.H., Barres, B.A., and Stevens, B. (2012). The complement system: an unexpected role in synaptic pruning during development and disease. Annu. Rev. Neurosci. *35*, 369–389.

Stevens, B., Allen, N.J., Vazquez, L.E., Howell, G.R., Christopherson, K.S., Nouri, N., Micheva, K.D., Mehalow, A.K., Huberman, A.D., Stafford, B., et al. (2007). The classical complement cascade mediates CNS synapse elimination. Cell *131*, 1164–1178.

Steward, O., and Schuman, E.M. (2001). Protein synthesis at synaptic sites on dendrites. Annu. Rev. Neurosci. *24*, 299–325.

Takeuchi, Y., Asano, H., Katayama, Y., Muragaki, Y., Imoto, K., and Miyata, M. (2014). Large-scale somatotopic refinement via functional synapse elimination in the sensory thalamus of developing mice. J. Neurosci. *34*, 1258–1270.

Thoreen, C.C., Chantranupong, L., Keys, H.R., Wang, T., Gray, N.S., and Sabatini, D.M. (2012). A unifying model for mTORC1-mediated regulation of mRNA translation. Nature *485*, 109–113.

Truitt, M.L., Conn, C.S., Shi, Z., Pang, X., Tokuyasu, T., Coady, A.M., Seo, Y., Barna, M., and Ruggero, D. (2015). Differential Requirements for eIF4E Dose in Normal Development and Cancer. Cell *162*, 59–71.

Tsukiyama-Kohara, K., Poulin, F., Kohara, M., DeMaria, C.T., Cheng, A., Wu, Z., Gingras, A.-C., Katsume, A., Elchebly, M., Spiegelman, B.M., et al. (2001). Adipose tissue reduction in mice lacking the translational inhibitor 4E-BP1. Nat. Med. *7*, 1128–1132.

Turney, S.G., and Lichtman, J.W. (2012). Reversing the outcome of synapse elimination at developing neuromuscular junctions in vivo: evidence for synaptic competition and its mechanism. PLoS Biol. *10*, e1001352.

Voyvodic, J.T. (1987). Development and regulation of dendrites in the rat superior cervical ganglion. J. Neurosci. *7*, 904–912.

Wang, D.O., Martin, K.C., and Zukin, R.S. (2010). Spatially restricting gene expression by local translation at synapses. Trends Neurosci. *33*, 173–182.

Wang, H., Liu, H., and Zhang, Z.W. (2011). Elimination of redundant synaptic inputs in the absence of synaptic strengthening. J. Neurosci. *31*, 16675–16684.

Wells, D.G., Richter, J.D., and Fallon, J.R. (2000). Molecular mechanisms for activity-regulated protein synthesis in the synapto-dendritic compartment. Curr. Opin. Neurobiol. *10*, 132–137.

Wong, R.O.L., and Ghosh, A. (2002). Activity-dependent regulation of dendritic growth and patterning. Nat. Rev. Neurosci. *3*, 803–812.

Xu, W., Gelber, S., Orr-Urtreger, A., Armstrong, D., Lewis, R.A., Ou, C.-N., Patrick, J., Role, L., De Biasi, M., and Beaudet, A.L. (1999). Megacystis, mydriasis, and ion channel defect in mice lacking the α3 neuronal nicotinic acetylcholine receptor. Proc. Natl. Acad. Sci. USA *96*, 5746–5751.

Yasuda, M., Johnson-Venkatesh, E.M., Zhang, H., Parent, J.M., Sutton, M.A., and Umemori, H. (2011). Multiple forms of activity-dependent competition refine hippocampal circuits in vivo. Neuron *70*, 1128–1142.

Zhang, L.I., and Poo, M.M. (2001). Electrical activity and development of neural circuits. Nat. Neurosci. *4* (*Suppl*), 1207–1214.

Zou, D.-J., Feinstein, P., Rivers, A.L., Mathews, G.A., Kim, A., Greer, C.A., Mombaerts, P., and Firestein, S. (2004). Postnatal refinement of peripheral olfactory projections. Science *304*, 1976–1979.

Cell Reports, Volume *23*

Supplemental Information

Removing 4E-BP Enables Synapses to Refine without Postsynaptic Activity

Yumaine Chong, Natasha Saviuk, Brigitte Pie, Nathan Basisty, Ryan K. Quinn, Birgit Schilling, Nahum Sonenberg, Ellis Cooper, and A. Pejmun Haghighi

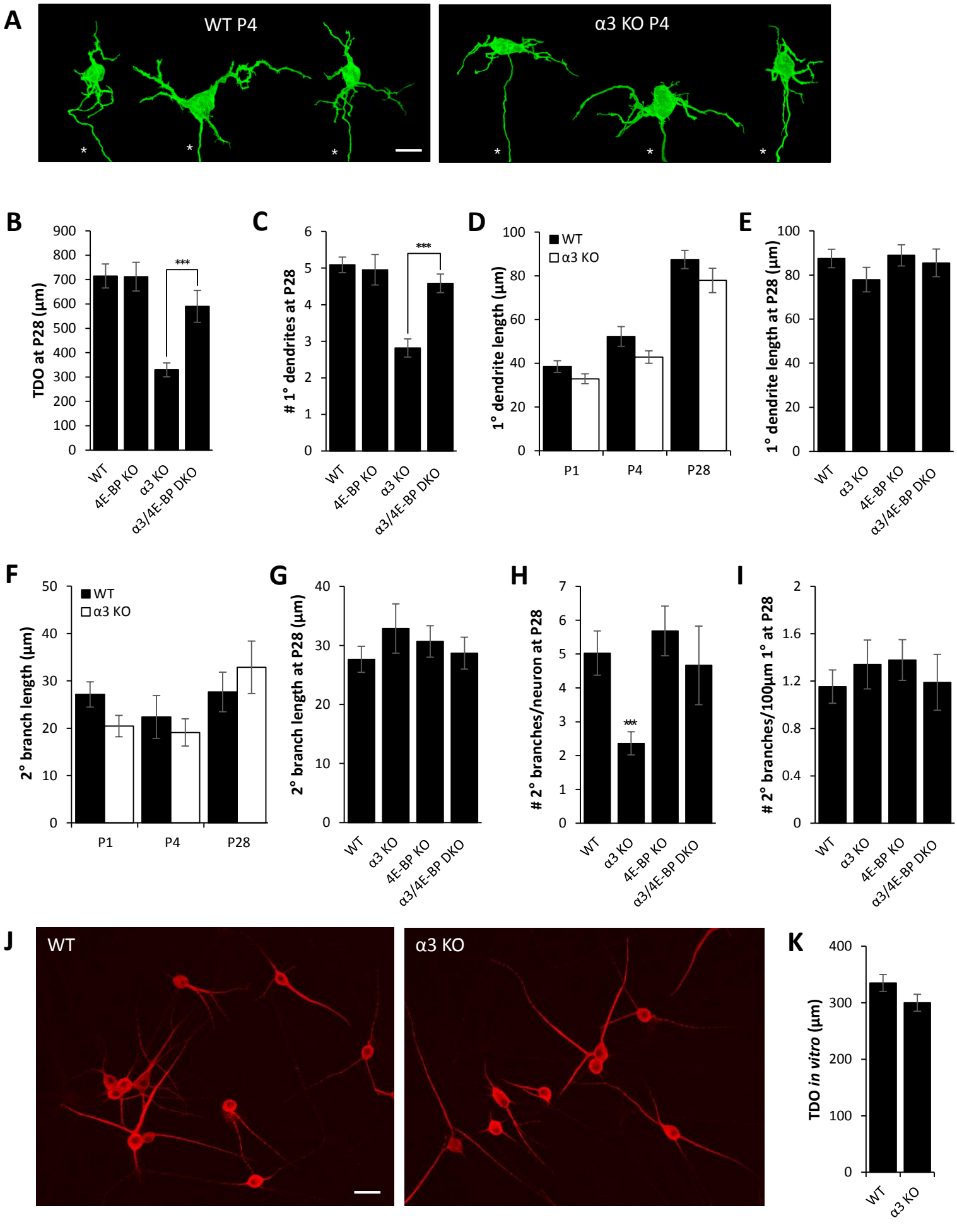

Fig. S1 Chong *et al.*

Figure S1. Dendritic morphology of WT, α3 KO, 4E-BP KO, and α3/4E-BP DKO SCG neurons. Related to Figure 3.

Lipophilic dye, DiO, was applied to the postganglionic nerve of the SCG to sparsely label a random subset of individual SCG neurons. Neurons were imaged with confocal microscopy and reconstructed in 3D to quantify the length and number of dendritic branches.

(**A**) Maximum intensity projections of DiO-labelled P4 neurons from WT (left) and α3 KO (right) SCG. All neurons are shown at the same scale. Scale bar, 20 μm; axons are marked by an asterisk.

(**B**&**C**) P28 SCG neuron; (**B**) Average total dendritic outgrowth, (**C**) average number of primary dendrites.

(**D**) Average length of primary dendrites at P1, P4, and P28; WT (filled columns), α3 KO (open columns).

(**E**) Average length of primary dendrites per P28 SCG neuron.

(**F**) Average length of secondary dendrites at P1, P4, and P28; WT (filled columns), α3 KO (open columns).

(**G**-**I**) P28 SCG neuron; (**G**) Average length of secondary branches, (**H**) average number of secondary branches, (**I**) average number of secondary branches normalized to 100μm length of primary dendrite.

Error bars represent ± SEM; ***p<0.001. WT: for P1, n=23 neurons (10 mice); for P4, n=28 neurons (10 mice); and for P28, n=34 neurons (12 mice). α3 KO: for P1, n=21 neurons (10 mice); for P4, n=24 neurons (10 mice); and for P28, n=36 neurons (14 mice). For 4E-BP KO at P28, n=22 neurons (8 mice). For α3/4E-BP DKO at P28, n=24 neurons (6 mice).

(**J**) Immunostaining for MAP-2 labels dendrites of cultured P4 neurons (14 days *in vitro*) from WT SCG (left) and α3 KO SCG (right). Scale bar, 40 μm.

(**K**) Average total dendritic outgrowth per cultured SCG neuron after 14 days *in vitro*.

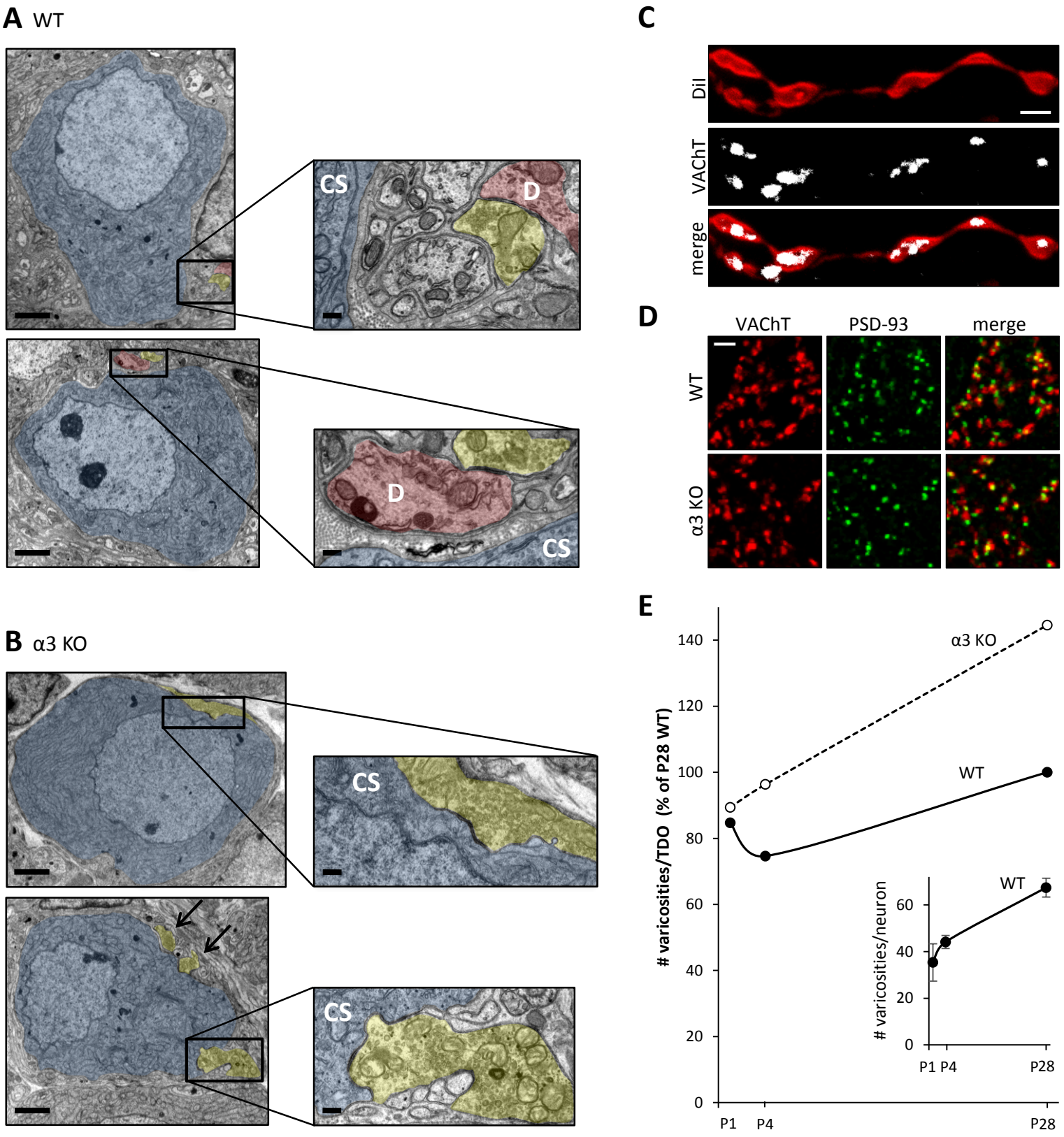

Fig. S2 Chong *et al.*

Figure S2. Varicosities in α3 KO SCG are larger and border the cell soma more frequently than in WT SCG. Varicosities have VAChT, which colocalizes with PSD-93. Related to Figure 3.

(**A**&**B**) Sample electron micrographs show cell somas (blue), varicosities (yellow) and dendrites (red). Low power images (left) show the cell soma in its entirety; scale bar, 2 μm. Boxed regions are magnified on the right; scale bar, 0.2 μm. In WT sections (A), varicosities were predominantly found in the neuropil between cell somas. In α3 KO sections (B), varicosities bordering the cell soma were often larger than those in WT sections. Arrows in the lower α3 KO micrograph point to two additional varicosities on the cell soma.

(**C**) Confocal image of a DiI-labeled axon (red), immunostained for VAchT. Varicosities are positive for VAChT (white). Scale bar, 2 μm.

(**D**) Confocal images SCG sections immunostained for VAChT (red) and PSD-93 (green). Over 90% of presynaptic VAChT puncta are colocalized with postsynaptic PSD-93 puncta; scale bar, 3 μm. Images were selected from the neuropil area between cell bodies where synapse concentration is highest.

(**E**) Number of varicosities normalized to total dendritic outgrowth for WT neurons and α3 KO neurons at P1, P4 and P28. Inset shows the number of varicosities for WT SCG neurons, which increases over 2-fold from P1 to P28. For P1, n=6 neurons (3 mice); for P4, n=9 neurons (5 mice); and for P28, n=10 neurons (4 mice).

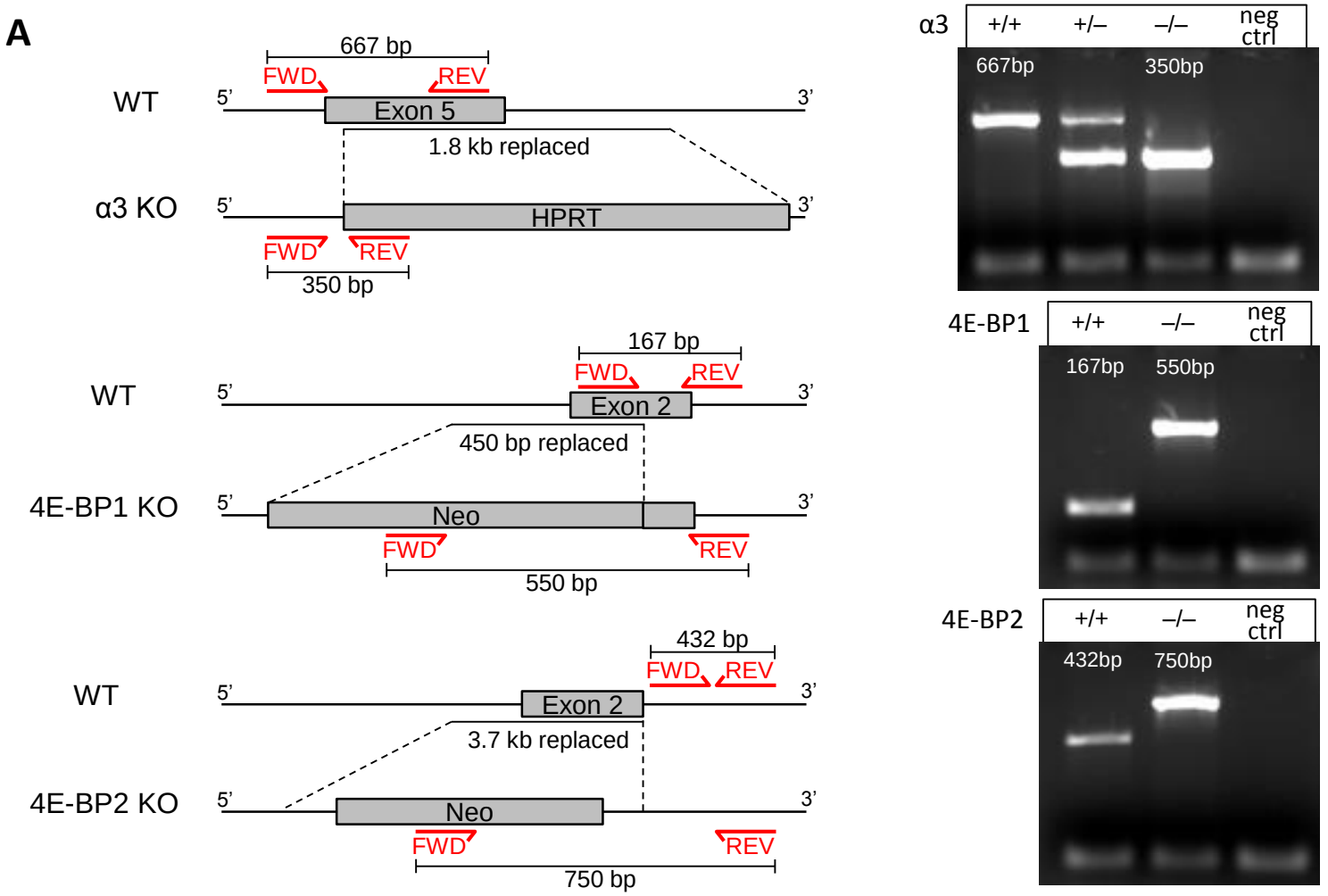

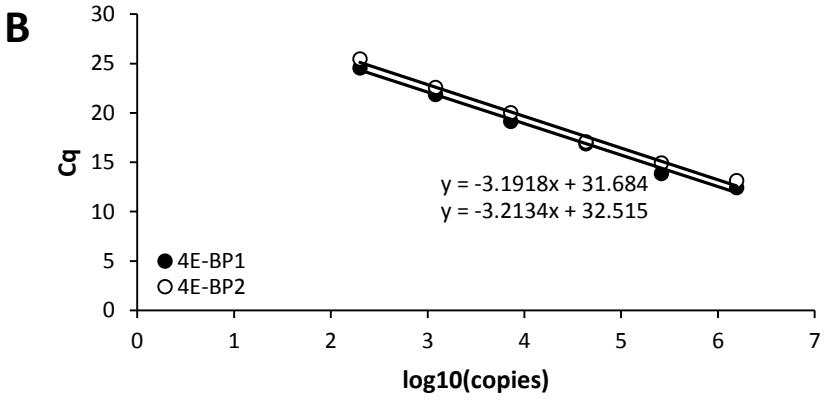

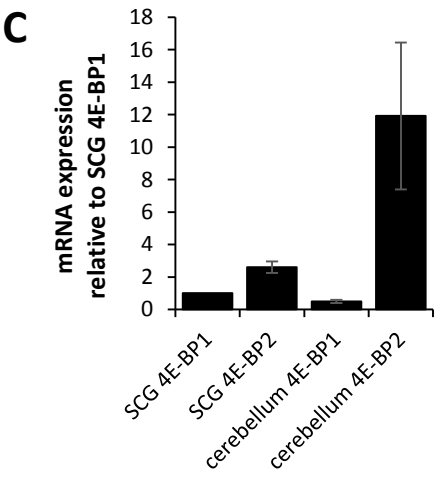

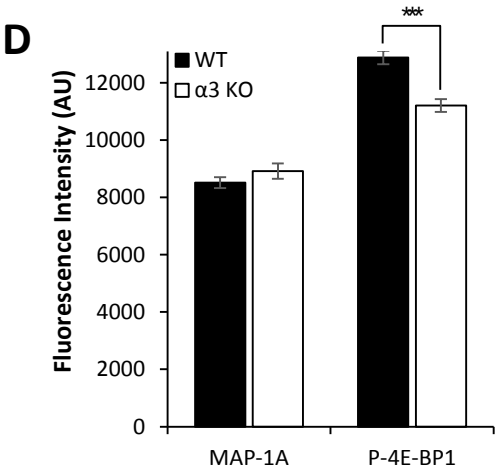

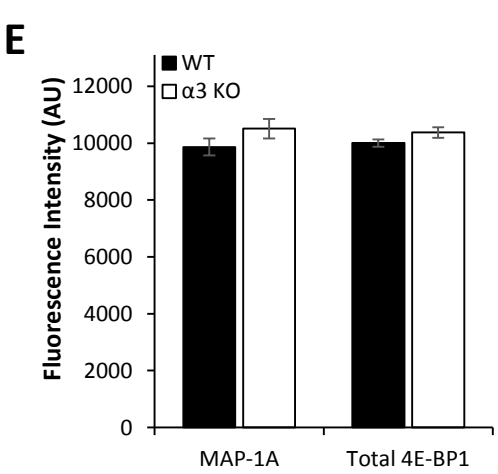

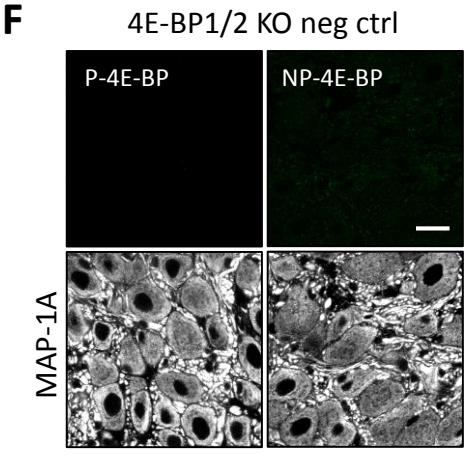

Fig. S3 Chong *et al.*

Figure S3. 4E-BP1 and 4E-BP2 are both expressed in SCG, and WT SCG has higher levels of P-4E-BP1 than α3 KO SCG. Related to Figure 4.

(**A**) Genotypes of α3, 4E-BP1 and 4E-BP2 KO mice were determined by PCR. Left: Diagrams show WT and KO alleles for α3, 4E-BP1 and 4E-BP2. The binding locations of the primers used for genotyping for indicated in red. See Table S1 for primer sequences. Right: Figures show PCR amplicons run on an agarose gel; numbers above each band correspond to expected amplicon sizes.

(**B**&**C**) Standard curves were generated from a 6-point serial dilution of known copy numbers of 4E-BP1 and 4E-BP2 cDNA (B). Primer pairs for each transcript have a near-identical amplification efficiency. Overlapping standard curves indicate that both primer pairs function in a comparable manner. Average 4E-BP1 and 4E-BP2 mRNA levels expressed in SCG and cerebellum (C). The ratios of 4E-BP1:4E-BP2 mRNA levels are ~1/2.6 in SCG and ~1/24 in cerebellum. For SCG, n=8 mice and for cerebellum n=8 mice. See Table S2 for primer sequences.

(**D**&**E**) Mean fluorescence intensity of MAP-1A, P-4E-BP1 and total 4E-BP1 in WT and α3 KO SCG; (**D**) MAP-1A and P-4E-BP1 and (**E**) MAP-1A and total 4E-BP1.

Error bars represent ± SEM; ***p<0.001. For B, WT n=120 neurons (3 mice), α3 KO n=120 neurons (3 mice). For C, WT n=140 neurons (3 mice), α3 KO n=140 neurons (3 mice).

(**F**) 4E-BP1/2 KO SCG at P28 were immunostained for phospho-4EBP1 and total 4E-BP1 (green) and MAP-1A (white) to test for non-specific binding of antibodies. Scale bar, 20 μm.

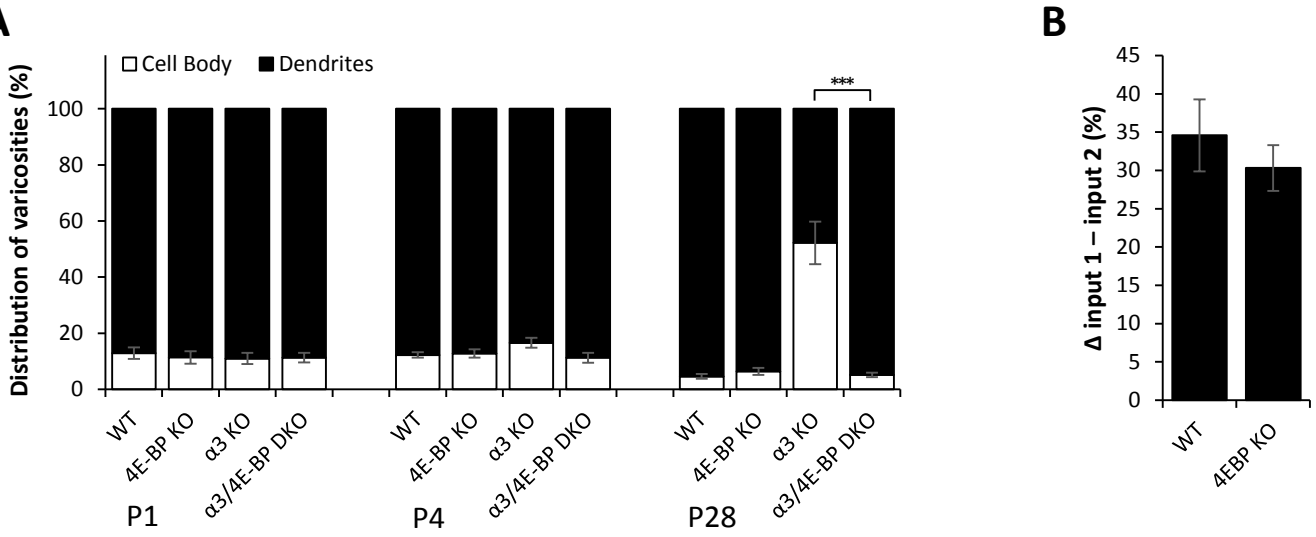

Fig. S4 Chong *et al.*

Figure S4. The distribution of varicosities is restored to the dendrites in α3/4E-BP DKO mice at P28. Related to Figure 5.

(**A**) Average distribution of varicosities on the cell body (open) and dendrites (filled) in WT, 4E-BP KO, α3 KO, and α3/4E-BP DKO SCG at P1, P4 and P28.

(**B**) The average difference in strength between the strongest and second strongest inputs in WT and 4E-BP KO SCG at P28, expressed as a percentage of the maximum compound EPSP.

Error bars represent ± SEM; ***p<0.001. In A, WT: for P1, n=6 neurons (3 mice); for P4, n=9 neurons (5 mice); and for P28, n=10 neurons (4 mice). 4E-BP: for P1 n=6 neurons (3 mice); for P4, n=7 neurons (5 mice); and for P28, n=10 neurons (4 mice). α3 KO: for P1 n=6 (5 mice); for P4, n=10 neurons (4 mice); and for P28, n=11 neurons (4 mice). α3/4E-BP DKO: for P1 n=6 (3 mice); for P4, n=7 neurons (4 mice); and for P28, n=10 neurons (4 mice). In B, WT n=36 neurons, 4E-BP n=33 neurons.

A Molecular Function

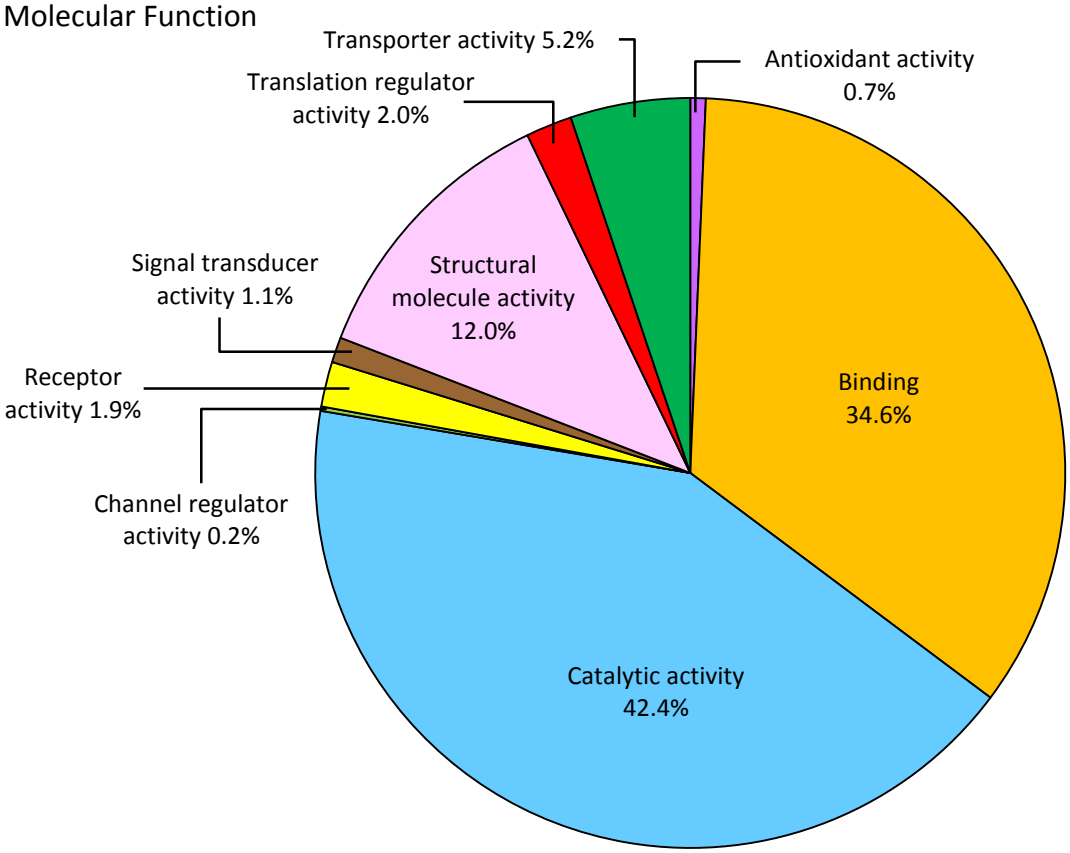

B Protein Class

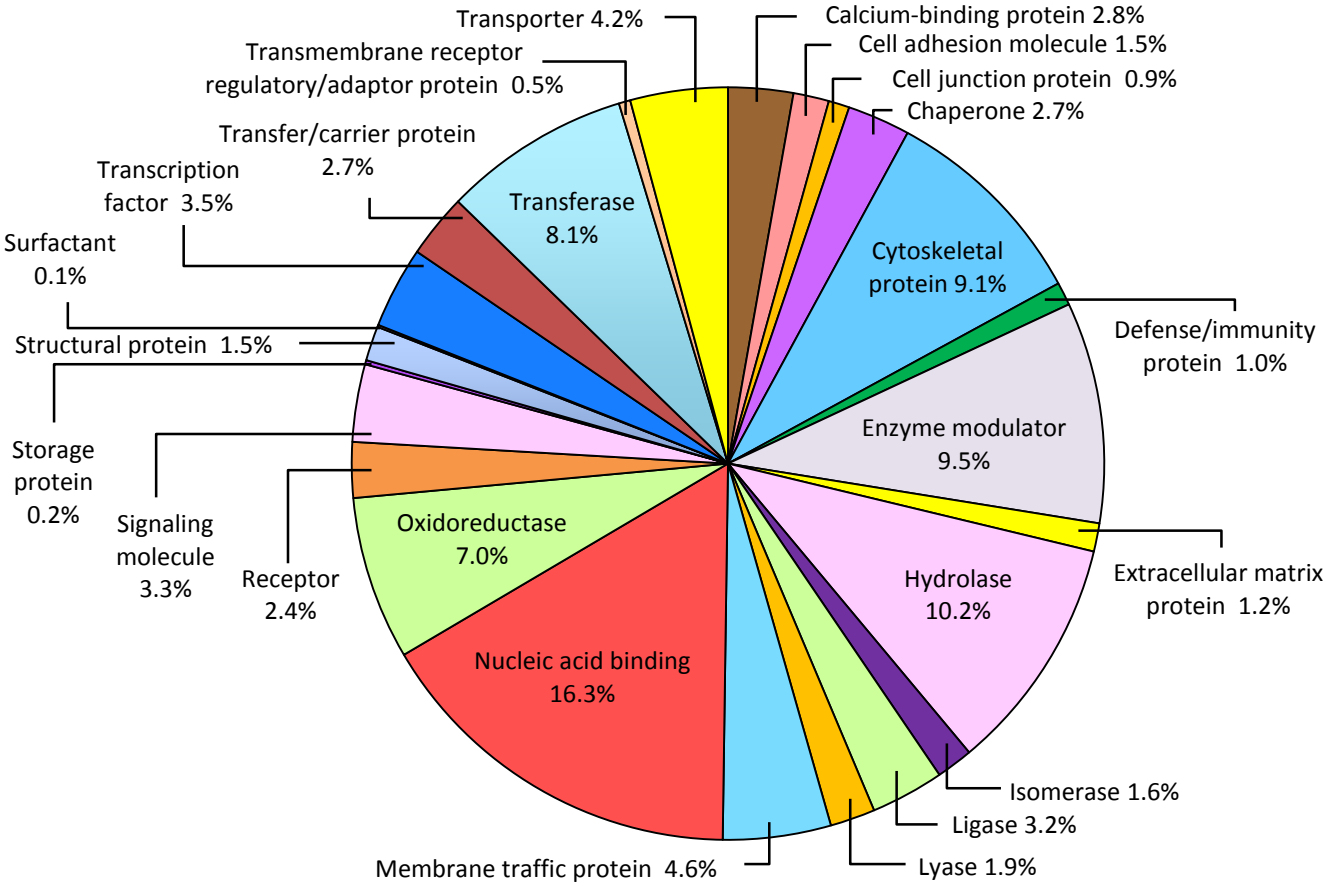

Fig. S5 Chong *et al.*

Figure S5. The classification of 2100 proteins identified in P28 WT SCG. Related to Figure 5.

(**A**&**B**) Pie charts showing the classification of 2100 proteins identified in P28 WT SCG into (**A**) molecular functions, and (**B**) protein classes. Proteins were identified using a data-independent acquisition SWATH MS/MS workflow and classified according to Gene Ontology (GO) terms and PANTHER protein classes.

Gene		Primer sequence (5’ – 3’)
α3	WT	FWD: GTT ATG CAC GGG AAG CCA GGC TGG REV: GAC TGT GAT GAC GAT GGA CAA GGT GAC
	KO	FWD: GTT ATG CAC GGG AAG CCA GGC TGG REV: TGG CGC GAA GGG ACC ACC AAA GAA CGG
4E-BP1	WT	FWD: GAT GGA GTG TCG GAA CTC ACC REV: GAC CTG GAC AGG ACT CAC CGC
	KO	FWD: GCA TCG AGC GAG CAC GTA CTC REV: GAC CTG GAC AGG ACT CAC CGC
4E-BP2	WT	FWD: GGG TGG ACT GTC GGT CTT CTG REV: CAG CAC CTG GTC ATA GCC GTG
	KO	FWD: GCA TCG AGC GAG CAC GTA CTC REV: CAG CAC CTG GTC ATA GCC GTG

Table S1. Forward and reverse primer sequences used for PCR genotyping of α3, 4E-BP1 and 4E-BP2 KO mice. Related to Figure 4 and Supplemental Figure S3.

Gene	Primer sequence (5’ – 3’)
4E-BP1	FWD: AGC CAT TCC TGG GGT CAC TA REV: ATC ATT GCG TCC TAC GGC TG
4E-BP2	FWD: CTG CCC TCT GCC CAG TTA AG REV: TGC TTG GAG ACT GCC CTA GA
GAPDH	FWD: CTG GCA TGG CCT TCC GTG TT REV: TAC TTG GCA GGT TTC TCC AGG CG
18S	FWD: GCA ATT ATT CCC CAT GAA CG REV: GGG ACT TAA TCA ACG CAA GC

Table S2. Forward and reverse primer sequences used for qPCR. Related to Figure 4 and Supplemental Figure S3.

Table S3. Z-scores, z-score ratios, and q-values used to generate the heatmap in Figure 5.

Gene	z-score			α3 KO : WT		α3/4E-BP DKO : WT	
	WT	α3 KO	α3/4E-BP DKO	Ratio	q-value	Ratio	q-value
Acly	1250.5	1942.25	1874.97	1.55	1.08E-07	1.5	1.81E-06
Anp32b	399.8	610.7	617.01	1.53	0.048	1.54	0.018
Anxa5	2915.33	5223.19	5387.85	1.79	1.16E-15	1.85	2.49E-14
Ap2a2	247.34	358.36	340.03	1.45	0.021	1.37	0.278
Apoa1	2924.02	5262.45	8421.88	1.8	1.77E-04	2.88	4.41E-09
Apod	127.19	210.8	257.8	1.66	0.037	2.03	0.157
Arhgdia	1602.77	2313.65	2066.32	1.44	3.34E-04	1.29	0.008
Atic	872.33	1324.71	1120.78	1.52	0.007	1.28	0.002
Atp5a1	3152.5	1567.74	1882.91	0.5	0.007	0.6	2.78E-08
Atp5b	182.91	62.09	121.81	0.34	0.028	0.67	0.238
Atp5c1	413.57	288	293.54	0.7	0.008	0.71	0.305
Atp5j	362.61	208.97	240.97	0.58	0.026	0.66	0.229
Cadm2	149.53	332.15	264.36	2.22	0.006	1.77	0.319
Cda	246.78	369.41	184.57	1.5	0.016	0.75	0.028
Cend1	212.73	101.83	123.41	0.48	0.002	0.58	0.001
Ckb	2518.17	1231.73	1622.96	0.49	0.002	0.64	0.024
Col28a1	1191.56	824.37	1487.35	0.69	0.002	1.25	0.087
Cox5b	967.24	593.47	559.63	0.61	0.033	0.58	0.013
Cpne2	49.04	89.34	112.22	1.82	0.024	2.29	0.277
Ctsb	1064.6	673.32	805.34	0.63	3.00E-05	0.76	0.002
Ddc	943.57	1525.27	1254.44	1.62	1.48E-04	1.33	0.422
Elavl2	640.62	350.58	379.97	0.55	0.005	0.59	0.002
Epdr1	487.08	774.35	549.25	1.59	0.01	1.13	0.571
Fasn	1719.25	2196.54	2206.74	1.28	2.30E-09	1.28	2.3E-06
Fbl	283.6	359.22	301.55	1.27	0.021	1.06	0.532
Fbxo2	451.87	639.45	484.52	1.42	0.01	1.07	0.311
Fkbp1a	1219.7	2053.61	1936.77	1.68	0.001	1.59	2.02E-04
Gda	403.7	980.37	1204.14	2.43	0.002	2.98	6.62E-11
Gmppb	411.7	771.64	458.94	1.87	0.006	1.11	0.346
Gpi	523.14	694.22	619.6	1.33	0.004	1.18	0.515
Gpx1	838.91	1226.97	1345.89	1.46	0.029	1.6	0.097
Hist1h1a	300.51	550.38	807.74	1.83	0.008	2.69	0.007
Hist1h1b	324.5	563.9	723.3	1.74	0.044	2.23	3.50E-05
Hist1h1c	2075.08	3307.83	3830.5	1.59	0.044	1.85	0.001
Hist1h1e	2120.81	2958.81	3303.83	1.4	0.006	1.56	0.007
Hist2h2aa1	225.09	295.46	455.17	1.31	0.029	2.02	0.204
Hmgn2	50.61	98.82	106.94	1.95	2.00E-05	2.11	0.054
Ina	1663.29	1026.06	1130.21	0.62	4.31E-04	0.68	0.079
Krt1	1236.6	548.35	811.24	0.44	1.74E-08	0.66	1.23E-04
Krt10	1498.45	724.91	1171.19	0.48	0.02	0.78	0.116
Krt2	632.05	394.83	448.31	0.62	0.014	0.71	0.187
Krt6a/6b	1032.29	415.01	666.1	0.4	0.005	0.65	0.355
Krt77	1285.23	588.03	838.06	0.46	4.48E-04	0.65	0.003
Krt79	378.5	197.18	252.02	0.52	0.001	0.67	8.00E-06
Lnp	137.96	76.22	85.59	0.55	0.012	0.62	0.186
Mif	1907.87	2727.7	2745.68	1.43	0.008	1.44	0.034
Mtco2	439.93	227.52	296.75	0.52	0.03	0.67	0.343
Myl1	615.39	275.81	371.95	0.45	0.001	0.6	0.003

Table S3 (continued).

Naca	751.28	557.81	556.84	0.74	0.01	0.74	0.062
Ncald	229.29	97.49	96.16	0.43	3.66E-05	0.42	0.005
Nefh	950.5	432.24	414.24	0.45	8.20E-08	0.44	1.43E-08
Nefl	3029.67	1977.93	2040.21	0.65	9.35E-11	0.67	1.33E-09
Npy	129.9	33.06	50.79	0.25	0.039	0.39	0.413
Nudt3	105.6	202.96	179.44	1.92	0.023	1.7	0.427
Omp	594.07	761.61	763.64	1.28	0.028	1.29	0.127
Oxct1	1116.11	814.54	920.08	0.73	0.001	0.82	0.044
Pabpc1	898.41	1240.42	993.25	1.38	0.038	1.11	0.066
Pcnp	237.34	373.99	333.01	1.58	0.041	1.4	0.602
Pdhx	255.47	162.62	208.66	0.64	0.033	0.82	0.349
Pfn2	240.89	327.03	286.13	1.36	0.011	1.19	0.241
Pgp	128.23	190.64	164.13	1.49	0.034	1.28	0.289
Pnp	329.19	495.64	507.25	1.51	0.007	1.54	0.004
Ppia	2699.2	3405.2	3383.34	1.26	5.79E-05	1.25	2.00E-05
Prdx2	6025.87	7602.19	6347.94	1.26	8.33E-05	1.05	0.648
Psma6	581.44	735.78	694.06	1.27	0.014	1.19	0.248
Ptma	232.69	362.75	233.55	1.56	4.45E-04	1	0.386
Pura	1701.36	1194.41	1250.4	0.7	1.92E-04	0.73	0.007
Rbm3	259.32	519.76	567.58	2	0.039	2.19	0.099
Rps14	659.08	897.3	733.44	1.36	0.013	1.11	0.626
Rps5	762.55	561.21	515.19	0.74	0.015	0.68	1.08E-05
Selenbp1	260.2	353.64	394.6	1.36	0.013	1.52	1.70E-05
Serpina1b	377.23	511.03	604.04	1.35	1.20E-05	1.6	0.001
Serpina3k	621.93	927.09	629.82	1.49	0.034	1.01	0.011
Snd1	677.49	856.72	780.93	1.26	0.004	1.15	0.068
Stoml3	268.68	403.21	251.51	1.5	0.039	0.94	0.442
Th	1267.48	896.7	778.87	0.71	0.031	0.61	0.007
Thy1	816	573	489.42	0.7	0.005	0.6	2.02E-04
Tmsb10	3240.45	4483.99	3968.66	1.38	0.008	1.22	0.652
Tpt1	403.12	507.3	394.21	1.26	0.036	0.98	0.403
Tuba1b	1513.21	2513.96	2299.94	1.66	8.81E-08	1.52	5.98E-07
Uqcrc1	666.74	483.92	488.96	0.73	0.007	0.73	0.049
Ybx1	81.76	112.96	107.04	1.38	0.049	1.31	0.062
Ywhae	732.18	1075.49	1099.8	1.47	4.79E-09	1.5	6.02E-06

Contact for Reagent and Resource Sharing

Further information and requests for resources and reagents should be directed to and will be fulfilled by the Lead Contacts, Ellis Cooper (Ellis.Cooper@McGill.ca) or Pejmun Haghighi (phaghighi@buckinstitute.org).

Experimental Model and Subject Details

Mice

Mice with a deletion in the alpha 3 nicotinic subunit gene (Xu *et al*., 1999; referred to as α3 KO) were maintained on an outcrossed background (Krishnaswamy and Cooper, 2009). Briefly, inbred C57BL/6J α3+/- mice were mated to CD-1 WT mice and F1 α3+/- heterozygotes were used as breeders to produce α3 KO mice and WT littermates on a mixed C57BL/6J x CD-1 background. A series of crosses were performed between 4EBP1/2-/- mice (Tsukiyama-Kohara *et al*., 2001; Banko *et al*., 2005; provided by Dr. Nahum Sonenberg, McGill University) and α3 KO mice to generate 4EBP1/2-/-; α3-/- mice (referred to as α3/4E-BP DKO) on a mixed C57BL/6J x CD-1 background. Genotypes for all three genes were determined by PCR (**Supplemental Figure S3A**). Experiments were conducted on both male and female mice and all procedures for animal handling were carried out according to the guidelines of the Canadian Council on Animal Care.

Primary Neuronal Cultures

SCG neurons were cultured as described in Rassadi *et* al., 2005. Briefly, SCG were dissected from P4 α3 KO or WT littermates under sterile conditions. Ganglia were dissociated at 37°C in trypsin (1mg/mL; Worthington, Freehold, NJ) dissolved in 1X HBSS pH 7.4, washed with 1X HBSS, and plated on laminin-coated coverslips in growth media. The growth media consists of L-15 media supplemented with vitamins, cofactors, penicillin–streptomycin, 5% rat serum, and NGF (50 ng/ml). Cultures were treated with cytosine arabinoside (10μm; Sigma Millipore, St. Louis, MO) from days 2 to 4 to eliminate non-neuronal cells, and fed every 3 days.

Method Details

Electrophysiological Recordings

SCG were acutely dissected in oxygenated Tyrode's solution supplemented with glucose (5.6 mM) and choline (0.01 mM) (pH = 7.3–7.4), pinned down with minutia pins on a Sylgard-coated petri dish, mounted on a fixed stage, and viewed through a dissecting microscope (SMZ-10; Nikon, Tokyo, Japan). To record the nerve-evoked postganglionic compound action potential (CAP), we connected the preganglionic nerve to a stimulator (Stimulus Isolator, model A365; World Precision Instruments, Sarasota, FL) with a suction electrode and recorded from the postganglionic trunk with a suction electrode connected to differential amplifier (DP-301; Warner Instruments); the signals were amplified (1000 X), filtered at 300 Hz and 10kHz, and digitized at 10kHz.

To record intracellularly from ganglion cells, we used 80–120 mΩ glass microelectrodes (G150F-4; Warner Instruments, Hamden, CT) made with a DMZ universal puller (Zeitz Instruments, Munich, Germany). Stable intracellular recordings were achieved with a high inertial precision microdrive (Inchworm 8200; EXFO, Quebec, Canada) attached to a micromanipulator (SM11; Narshige, Tokyo, Japan) that drove the electrode through the ganglion. The recording electrode was filled with 1M KAc and connected by a thin silver chlorided wire to the head stage of an Axoclamp 2A amplifier (Axon Instruments, Union City, CA) used in current-clamp mode, and depolarizing or hyperpolarizing constant current pulses were applied through the recording electrode. Membrane voltages were filtered at 3kHz (low-pass cutoff) and 1Hz (high-pass cutoff) and digitized at 50 kHz. On-line stimulation and data acquisition were done with N-Clamp (Neuromatic, UK) and off-line data analysis was performed using Igor Pro software (WaveMetrics, Lake Oswego, OR). To measure dendrites on Ad-α3 infected neurons, intracellular electrodes (60–70 mΩ) were filled with 10mM Alexa Fluor 488 hydrazide (Thermo Fisher Scientific, Waltham, MA) in 200mM KCl.

To measure the convergence of preganglionic axons innervating a sympathetic neuron, the preganglionic nerve was stimulated with voltages of increasing strength while holding the neuron at ~ -90 mV to prevent EPSPs from triggering action potentials. In some experiments, we also included QX314 in the recording electrode to prevent action potentials. At maximal stimulus strength, the $EPSP_{max}$ is the sum of the EPSPs evoked by each of the axons innervating that neuron (Eq. 1). Increasing the strength of the stimulus to the preganglionic nerve activates axons of different threshold which results in discrete jumps in the amplitude of the EPSPs. We used these discrete jumps as a measure of the number of axons innervating the neuron. To isolate the EPSP evoked by individual axons, we averaged at least 10 traces for each discrete jump and subtracted the average EPSP evoked by that axon and all axons of lower threshold from the average EPSP evoked only by axons of lower threshold (Eq. 2).

For N axons innervating a neuron,

$$\mathrm{EPSP}_{max} = \sum_{n=1}^{N} \mathrm{EPSP}_n \qquad \text{Eq. 1}$$

To isolate the $EPSP_n$ evoked by axon n,

$$\mathrm{EPSP}_n = \sum_{n=1}^{n} \mathrm{EPSP}_n - \sum_{n=1}^{n-1} \mathrm{EPSP}_{n-1} \qquad \text{Eq. 2}$$

To calculate the disparity index, DI, for each neuron, we divided the standard deviation, SD, of the EPSPs by the mean EPSP (Hashimoto and Kano, 2003). (Eq. 3.)

$$DI = SD/M \qquad \text{Eq. 3}$$

$$SD = \sqrt{\frac{\sum_{n=1}^{N} (EPSP_n - M)^2}{N-1}}$$

$$M = \mathrm{EPSP}_{max}/N$$

Adenoviruses

Full-length α3 neuronal nAChR subunit cDNA was ligated into pAdTrack-synapsin 1 (Ad-α3/Syn), and replication-deficient viral vectors were made according to He *et al*. (1998), as described previously (Krishnaswamy and Cooper, 2009). The synapsin promoter was only active in SCG neurons for ~2 weeks; to overexpress α3 for longer times, we used the human ubiquitin C promoter (Schorpp *et al*., 1996). Viruses were titered in duplicate with Adeno-X Rapid Titer Kit, (Clontech Lab, Mountain View, CA).

We infected mice with either Ad-α3/Syn or Ad-α3/Ubi adenovirus at a concentration of ~10^7 pfu/mL diluted in 1X PBS. For P28 α3 KO or α3/4E-BP DKO and P60 α3 KO mice, 200-300 µL was injected into the tail vein (IV). For P0-1 pups, we injected ~50 µL into the temporal vein, and for P8-9 pups, we injected 100-150 µL into the intraperitoneal cavity (IP).

Lipophilic Tracer Labeling

We used lipophilic tracers DiI and DiO (Thermo Fisher Scientific) to sparsely label a random subset of preganglionic axons and postsynaptic neurons in the SCG. When used to quantify dendritic morphologies, this method is preferable to labelling with intracellular dye injection because it avoids selection bias for neurons with large cell bodies. Briefly, freshly dissected ganglia with intact pre- and post-ganglionic nerves were fixed in 1% PFA (pH 7.4) in 0.1M PB for 2 hours at room temperature (RT) and embedded in 3% agarose Type I-B (Sigma Millipore) dissolved in 1X PBS, and a razor blade was used to slice through the pre- and post- ganglionic nerves to expose a cross-sectional area of the nerve. Platinum wires were used to gently apply fine crystals of DiI to the preganglionic nerve, and DiO to the postganglionic

nerve. After labelling, ganglia were kept in the dark in 1X PBS for 5 - 6 days to allow for tracers to diffuse along the axons. Ganglia were sliced into 100 μm sections with the Compresstome VF-200 (Precisionary Instruments Inc., Greenville, NC) using a solid zirconia ceramic injector blade (Cadence Inc., Staunton, VA). Sections were either mounted with Vectashield (Vector Laboratories, Burlingame, CA) and immediately imaged, or first processed with immunohistochemistry before mounting and imaging.

Immunohistochemistry

SCG were fixed, embedded, and sliced into 100 μm sections with the Compresstome VF-200, as above. Fixation and blocking were performed at room temperature.

VAChT staining on DiO-labelled or Alexa Fluor 488-filled neurons: We immunostained for VAChT on DiO-labelled neurons in fixed sections, or on Alexa Fluor 488-filled neurons in ganglia that were then fixed in 1% PFA in 0.1M PB for 1 hr and sectioned. Sections were blocked in 10% normal donkey serum (DS) (Millipore), and 0.3% Tween 20 (Fisher Scientific) in 1X PBS (blocking solution) for 2 hr, and then, incubated in primary antibodies in blocking solution at 4°C for 48 hr, and then in secondary antibodies in 10% DS at RT for 2 hr, and imaged. Primary antibody: Rabbit anti-VAChT (1:3000; Synaptic Systems); Secondary antibody: Alexa Fluor 647 donkey anti-rabbit (1:500; Thermo Fisher Scientific).

P-4E-BP1, 4E-BP1 and MAP-1A staining: SCG were immediately fixed in 2% PFA in 0.1M PB with 5mM EGTA for 1 hr and then sectioned. Sections were blocked in 10% DS, 0.3% Tween 20 and 0.05% Triton X-100 in 1X PBS (blocking solution) for 1 hr and incubated in primary antibodies (P-4E-BP1 or 4E-BP1 with MAP-1A) in blocking solution at 4°C for 48 hours, then in secondary antibodies in 10% DS at RT for 1 hr, and mounted for imaging. WT and α3 KO samples were processed in parallel. Primary antibodies: Rabbit anti-P-4E-BP1 (1:600; Cell Signaling, Danvers, MA), rabbit anti-4E-BP1 (1:600; Cell Signaling), goat anti-MAP-1A (1:360; Santa Cruz Biotechnology, Dallas, TX); Secondary antibodies:

TRITC donkey anti-rabbit (1:500; Jackson ImmunoResearch Laboratories) and Alexa Fluor 647 donkey anti-goat (1:500; Thermo Fisher Scientific).

VAChT and PSD-93: SCG were immediately fixed in 2% PFA in 0.1M PB (pH 6) for 10 minutes and then sectioned. Sections were blocked in 10% DS, and 0.3% Tween 20 in 1X PBS (blocking solution) for 2 hr, then incubated in primary antibodies in blocking solution at 4°C for 48 hr, and then in secondary antibodies in 10% DS at RT for 1 hr, and imaged. Primary antibodies: Rabbit anti-VAChT (1:3000; Cell Signaling, Danvers, MA), mouse anti-PSD-93 (1:300; NeuroMab, Davis, CA); Secondary antibodies: Alexa Fluor 647 donkey anti-rabbit (1:500; Thermo Fisher Scientific) and Alexa Fluor 568 goat anti-mouse IgG1 (1:500; Thermo Fisher Scientific).

Immunocytochemistry

Cultured SCG neurons (14 days *in vitro*) were fixed and permeabilized with cold 100% methanol for 10 mins at -20°C, rinsed with 1X PBS, blocked in 10% DS in 1X PBS for 1 hr, incubated in primary antibody mouse anti-MAP-2 (1:500; Sigma Millipore) in blocking solution overnight at 4°C, then in secondary antibody Alexa Fluor 568 goat anti-mouse IgG1 (1:500; Thermo Fisher Scientific) for 1 hr at room temperature, and imaged.

Image Acquisition and Analysis

Images were acquired on an upright confocal microscope (BX-61W, Olympus) with a 60X, NA 1.42 PlanApo N oil-immersion objective at a scan speed of 8 μs/pixel and an image depth of 12 bits. Laser lines were activated sequentially to avoid bleed-through of signals. All analysis was performed with ImageJ (NIH, Bethesda, MD).

Dendrite analysis: Images of DiO-labelled neurons were acquired at a pixel size of 0.172 μm/pixel (1024 x 1024 pixels) and an optical thickness of 0.37 μm/slice. Only neurons with complete dendritic arbors and an identifiable axon were analyzed. For images of isolated neurons, we removed all DiO-labelled neurites

that were not connected to the neuron of interest, as determined from 3D reconstructions. To quantify the length and number of dendritic branches, we reconstructed neurons in 3D and used the Simple Neurite Tracer plugin (Longair *et al*., 2011) to trace dendrites. Primary dendrites were categorized as those directly leaving the cell body, while secondary branches extended off primary dendrites. Thin protrusions shorter than 5 µm were considered dendritic filopodia and not counted as branches. For neurons with a dendritic arbor that extended beyond one field of view, neighbouring z-stacks were acquired and stitched together with XuvTools (Emmenlauer *et al*., 2009).

Synaptic targeting: Images were acquired at a pixel size of 0.172 µm/pixel (1024 x 1024 pixels), and an optical thickness of 0.36 µm/slice. To examine synaptic targeting, we identified VAChT puncta located on a neuron of interest on each plane of a z-stack. VAChT puncta that co-localized with the DiO membrane label, were at least 0.5 µm in diameter, and spanned at least two optical slices were counted as putative synapses.

Preganglionic axonal targeting: Images were acquired at a pixel size of 0.188 µm/pixel (1024 x 1024 pixels), optical thickness was 0.4 µm/slice. To estimate the percentage of the cell body surface covered by an axon, on each plane of the cell body, we measured the circumference of the cell body (DiO labelled from postganglionic nerve), and the proportion of the cell body circumference occupied by an axon (DiI labelled from preganglionic nerve) on that plane. The total surface area was calculated from the circumference of the cell body on each plane multiplied by the optical thickness.

P-4E-BP1, 4E-BP1 and MAP-1A fluorescence intensity: A z-stack of 20 images were acquired at a pixel size of 0.22 µm/pixel (800 x 800 pixels), and optical thickness was 0.47 µm/slice. All image acquisition parameters (HV, gain, offset, laser power) were kept constant between samples. For intensity analysis, each stack was used to generate a summed z-projection. Regions of interest (ROI), each consisting of one neuronal cell body, excluding the nucleus, were selected from the MAP-1A channel. Average

fluorescence intensity for each ROI was measured from the MAP-1A channel, and ROI were transferred to the P-4E-BP1 or 4E-BP1 channel to measure the corresponding fluorescence intensity.

Proteomics

Chemicals: Acetonitrile and water were obtained from Burdick & Jackson (Muskegon, MI). Reagents for protein chemistry including iodoacetamide, dithiothreitol (DTT), ammonium bicarbonate, formic acid (FA), and urea were purchased from Sigma Aldrich (St. Louis, MO). Sequencing grade trypsin was purchased from Promega (Madison, WI). HLB Oasis SPE cartridges were purchased from Waters (Milford, MA).

Superior Cervical Ganglia Sample Preparation for Mass Spectrometry – Digestion: For mass spectrometric analysis isolated frozen ganglia tissue pellets in PBS from WT and 3 different knock-out mice, 4EBP-KO, alpha-3-KO, and 4EBP/ alpha-3–double KO (also referred to as DKO) were processed. Mice were four weeks old and 6 ganglia were pooled into one sample, with a total of 3 biological replicates per each of the mouse strain. Ganglia were re-suspended in PBS containing 1X Roche Protease and Phosphatase inhibitor cocktail and lysed using a bead-beater and sonication. Samples were concentrated using 3 kDa centrifugal filters and transferred into a solution of 8M urea/100 mM Tris pH 8, and protein quantitation was performed using a BCA Protein Assay Kit (Pierce #23225, Waltham, MA). An aliquot of 10-20 µg from each sample was then brought to equal volume with 100 mM Tris buffer at pH 8. The protein mixtures were reduced with 20 mM DTT (37°C for 1 hour), and subsequently alkylated with 40 mM iodoacetamide (30 minutes at RT in the dark). Samples were diluted 10-fold with 100 mM Tris pH 8.0 and incubated overnight at 37°C with sequencing grade trypsin (Promega) added at a 1:50 enzyme:substrate ratio (wt/wt). The peptide supernatants were then collected and desalted with Oasis HLB 30 mg Sorbent Cartridges (Waters #186003908, Milford, MA) (Keshishian et al. 2007), concentrated and re-suspended in a solution containing mass spectrometric 'Hyper Reaction Monitoring' peptide standards (HRM, Biognosys #Kit-3003, Switzerland) and 0.2% formic acid in water.

Mass Spectrometry: Samples were analyzed by reverse-phase HPLC-ESI-MS/MS using the Eksigent Ultra Plus nano-LC 2D HPLC system (Dublin, CA) combined with a cHiPLC System, which was directly connected to a quadrupole time-of-flight SCIEX TripleTOF 6600 mass spectrometer (SCIEX, Redwood City, CA). Typically, mass resolution in precursor scans was ~ 45,000 (TripleTOF 6600), while fragment ion resolution was ~15,000 in 'high sensitivity' product ion scan mode. After injection, peptide mixtures were transferred onto a C18 pre-column chip (200 µm x 6 mm ChromXP C18-CL chip, 3 µm, 300 Å, SCIEX) and washed at 2 µl/min for 10 min with the loading solvent (H_2O/0.1% formic acid) for desalting. Subsequently, peptides were transferred to the 75 µm x 15 cm ChromXP C18-CL chip, 3 µm, 300 Å, (SCIEX), and eluted at a flow rate of 300 nL/min with a 3 h gradient using aqueous and acetonitrile solvent buffers.

For spectral library building, initial data-dependent acquisitions (DDA) were carried out to obtain MS/MS spectra for the 30 most abundant precursor ions (100 msec per MS/MS) following each survey MS1 scan (250 msec), yielding a total cycle time of 3.3 sec as previously described (Kuhn et al. 2014; Schilling et al. 2012; Schilling et al. 2015). For collision induced dissociation tandem mass spectrometry (CID-MS/MS), the mass window for precursor ion selection of the quadrupole mass analyzer was set to ± 1 *m/z* using the Analyst 1.7 (build 96) software. Subsequently, for label-free relative quantification all study samples were analyzed by data-independent acquisitions (DIA), or specifically variable window SWATH acquisitions. In these SWATH acquisitions (Kuhn et al. 2014; Rardin et al. 2015), instead of the Q1 quadrupole transmitting a narrow mass range through to the collision cell, windows of variable width (5 to 90 *m/z*) are passed in incremental steps over the full mass range (*m/z* 400-1250). The cycle time of 3.2 sec includes a 250 msec precursor ion scan followed by 45 msec accumulation time for each of the 64 SWATH segments. The variable windows were determined according to the complexity of the typical MS1 ion current observed within a certain *m/z* range using a SCIEX 'variable window calculator' algorithm (i.e. more narrow windows were chosen in 'busy' *m/z* ranges, wide windows in *m/z* ranges with few eluting precursor ions)(Schilling, Gibson, and Hunter 2017). SWATH MS2 produces complex MS/MS spectra which are a composite of all the analytes within each selected Q1 m/z window.

Mass Spectrometric Data Processing and Bioinformatics: Mass spectrometric data from data dependent acquisitions was analyzed using the database search engine ProteinPilot (SCIEX 5.0)(Shilov et al. 2007) using the Paragon algorithm. The following sample parameters were used: trypsin digestion, cysteine alkylation set to iodoacetamide, urea denaturation, and species *Mus musculus*. Trypsin specificity was assumed as C-terminal cleavage at lysine and arginine. Processing parameters were set to "Biological modification" and a thorough ID search effort was used. All DDA data files were searched using the SwissProt 2016_07 database (species: *M. musculus*). For Protein Pilot searches, to assess and restrict rates of false positive peptide/protein identifications, we used the (PSPEP) tool available in ProteinPilot 5.0 (Shilov et al. 2007), which automatically creates a concatenated forward and reverse decoy database. For database searches, a cut-off peptide confidence value of 99 was chosen. The Protein Pilot false discovery rate (FDR) analysis tool PSPEP provided a global FDR of 1% and a local FDR at 1% in all cases.

SWATH acquisitions were quantitatively processed using the proprietary Spectronaut v11 (11.0.15038.2.22948) software (Bruderer et al. 2016) from Biognosys. Quantitative SWATH MS2 data analysis was based on extracted ion chromatograms (XICs) of 6-10 of the most abundant fragment ions in the identified spectra. Relative quantification was performed comparing different conditions (WT and KO mice) assessing fold changes for proteins from the investigated mouse lines. Typically ganglia were pooled from 3 mice (2 ganglia per mouse providing a total of 6 ganglia) into one pooled biological replicate sample, and three of such pooled biological replicates per each of the four mouse strains were investigated and compared. Significance was assessed using FDR corrected q-values<0.05. See Data Accession (below) for quantitative results from mass spectrometric SWATH analysis.

Data Accession: The supplementary files provide further insights into the quantitative SWATH results. All raw files are uploaded to the Center for Computational Mass Spectrometry, MassIVE, and can be downloaded using the following link: ftp://MSV000081386@massive.ucsd.edu (MassIVE ID number: MSV000081386 and password: winter; ProteomeXchange Accession PXD007141). Data uploads include

mass spectrometric details for proteins and peptides that were identified and quantified by mass spectrometric analysis.

Heatmap: To generate the heatmap in Figure 5, we first identified proteins that were expressed at significantly different levels between α3 KO and WT SCG (±1.25x at q-value <0.05). For each of the 83 proteins identified to be differentially expressed, we calculated the $\log_2$ z-score ratio between the expression level in α3 KO SCG and the corresponding level in WT SCG, and between α3/4E-BP DKO SCG and WT SCG. We plotted the ratios using the gplots package (https://cran.r-project.org/package=gplots) in R (http://www.R-project.org).

Ultrastructural studies

Ganglia were dissected and fixed in 2% PFA/2% glutaraldehyde in 0.1M PB for 30 minutes at room temperature, cut in half to improve penetration and fixed for an additional 90 minutes. After fixation, ganglia were rinsed with 0.1M PB for 30 minutes, and incubated in 1% osmium tetroxide/1.5% potassium ferricyanide in H_2O for 1 hour at room temperature. Ganglia were rinsed briefly with H_2O to remove osmium tetroxide, and dehydrated in a graded series of ethanol concentrations from 30% to 100%, where each interval lasted 10 minutes, with the 100% ethanol step repeated 3 times. After dehydration, ganglia were incubated in 100% propylene oxide for 15 minutes twice, and incubated in a propylene oxide/Embed812 mixture at a ratio of 1:1, 1:2, and 1:3 for 1 hour, 2 hours and overnight respectively, and polymerized in Embed812 at 60C for 24 hours. Thin sections of ganglia were cut on an ultramicrotome, stained with 2% aqueous uranyl acetate and 3% lead citrate, and viewed with a Philips (Holland) EM410 electron microscope. To capture digital images, we used a Megaview 2 cooled-CCD camera at 10C and a GraBIT digital input board with analySIS analysis software (Olympus).

4E-BP1 and 4E-BP2 mRNA expression

RNA extraction and qPCR validation was performed in accordance with the MIQE guidelines (Bustin *et al*., 2009; Taylor *et al*., 2010).

RNA extraction: SCG from P28 WT mice were dissected and immediately flash frozen in liquid nitrogen. For cerebellum, P28 WT mice were perfused with oxygenated aCSF made with DEPC-treated H_2O, the cerebella were quickly removed, and ~200μm of the dorsal surface (lobes ~VI –IX) was isolated to minimize contribution of granule cell layer, and immediately flash frozen in liquid nitrogen. Total RNA from SCG and cerebella were extracted in parallel using the RNeasy Mini Kit (Qiagen). Frozen tissue was homogenized (Polytron PT 2100, Kinematica, Luzern, Switzerland) in buffer RLT with β-mercaptoethanol. Homogenates were processed according to the RNeasy Mini Kit protocol, and included a DNase I (Qiagen) treatment step to avoid contamination from genomic DNA. RNA quantity and purity was assessed with a NanoDrop2000c (NanoDrop, Wilmington, DE), and RNA integrity was assessed by running 400ng on a gel. 260/230 and 260/280 values were consistently >2.0, and 28S and 18S rRNA bands were consistently clear and sharp, with the 28S band approximately twice as intense as the 18S band. Reverse transcription (iScript Reverse Transcription Supermix for RT-qPCR, Bio-Rad, Hercules, CA) was performed immediately after RNA extraction, and used 200ng of RNA per reaction volume of 20μL. No-reverse transcriptase controls were included for each reaction to test for contamination from genomic DNA. cDNA was stored at -20°C.

qPCR: qPCRs were performed using SsoFast EvaGreen (Bio-Rad) on the Eco Real-Time PCR System (Illumina, San Diego, CA). Cycling parameters were as follows: UDG incubation 2mins at 50°C; Polymerase activation 30s at 95°C; PCR cycling (5s at 95°C, 15s at 60°C) for 40 cycles. Standard curves were generated from an 8-point 4X serial dilution of a mixed sample of SCG and cerebellar cDNA to determine primer efficiencies. All primers were 90-100% efficient at an annealing temperature of 60°C. See Table S2 for primer sequences. To compare SCG and cerebellum, samples were normalized to the geometric mean of the reference genes GAPDH and 18S. The stability value determined by NormFinder (Andersen *et al*., 2004) for the combination of GAPDH and 18S was 0.351. To estimate a ratio between 4E-BP1 and 4E-BP2 mRNA levels, we first generated standard curves from a 6-point serial dilution of

known copy numbers of 4E-BP1 and 4E-BP2 cDNA to ensure that both primer pairs and respective amplicons respond in a near-identical manner. See Table S2 for primer sequences. Each reaction contained 4μL of 256X-diluted cDNA in a total reaction volume of 10μL. Samples were run in duplicates, and no-reverse transcriptase and no template controls consistently showed no amplification.

Quantification and Statistical Analysis

Values of n and p-values are reported in the Figures and corresponding figure legends. In all figures, error bars represent ± SEM, *$p<0.05$, ***$p<0.001$. To test for statistical differences between two samples, we used unpaired two-tailed t tests assuming equal variance. To test for statistical differences between three or more samples, we used a one-way ANOVA to determine if one or more samples were significantly different. If the p-value calculated from the F-statistic was less than 0.05, we used a post-hoc Tukey HSD test to identify which pairs of samples were significantly different from each other.

Andersen, C.L., Jensen, J.L., Ørntoft, T.F. (2004). Normalization of real-time quantitative reverse transcription-PCR data: a model-based variance estimation approach to identify genes suited for normalization, applied to bladder and colon cancer data sets. Cancer Research *64*, 5245-50.

Bruderer, R., Bernhardt, O.M., Gandhi, T., Reiter, L. (2016). High-precision iRT prediction in the targeted analysis of data-independent acquisition and its impact on identification and quantitation. Proteomics *16*: 2246–2256.

Bustin, S.A., Benes, V., Garson, J.A., Hellemans, J., Huggett, J., Kubista, M., Mueller, R., Nolan, T., Pfaffl, M.W., Shipley, G. L., Vandesompele, J., and Wittwer, C.T. (2009). The MIQE Guidelines: Minimum Information for Publication of Quantitative Real-Time PCR Experiments. Clinical Chemistry *55*, 611–622.

Emmenlauer, M., Ronneberger, O., Ponti, A., Schwarb, P., Griffa, A., Filippi, A., Nitschke, R., Driever, W., and Burkhardt, H. (2009). XuvTools: free, fast and reliable stitching of large 3D datasets. Journal of Microscopy *233*, 42–60.

Gillet, L.C., Navarro, P., Tate, S., Rost, H., Selevsek, N., Reiter, L., Bonner, R., Aebersold, R. (2012). Targeted data extraction of the MS/MS spectra generated by data-independent acquisition: a new concept for consistent and accurate proteome analysis. Mol Cell Proteomics *11*: O111 016717.

He, T.-C., Zhou, S., Da Costa, L.T., Yu, J., Kinzler, K.W., and Vogelstein, B. (1998). A simplified system for generating recombinant adenoviruses. Proceedings of the National Academy of Sciences *95*, 2509–2514.

Keshishian, H., Addona, T., Burgess, M., Kuhn, E., Carr, S.A. (2007). Quantitative, multiplexed assays for low abundance proteins in plasma by targeted mass spectrometry and stable isotope dilution. Mol Cell Proteomics *6*: 2212–2229.

Kuhn, M. L., Zemaitaitis, B., Hu, L.I., Sahu, A., Sorensen, D., Minasov, G., Lima, B.P., Scholle, M., Mrksich, M., Anderson, W.F., Gibson, B.W., Schilling, B., Wolfe, A.J. (2014). Structural, kinetic and proteomic characterization of acetyl phosphate-dependent bacterial protein acetylation. PLoS One *9*: e94816.

Longair, M.H., Baker, D.A., and Armstrong, J.D. (2011). Simple Neurite Tracer: open source software for reconstruction, visualization and analysis of neuronal processes. Bioinformatics *27*, 2453–2454.

Meyer, J.G., D'Souza, A.K., Sorensen, D.J., Rardin, M.J., Wolfe, A.J., Gibson, B.W., Schilling, B. (2016). Quantification of Lysine Acetylation and Succinylation Stoichiometry in Proteins Using Mass Spectrometric Data-Independent Acquisitions (SWATH). J Am Soc Mass Spectrom *27*: 1758–1771.

R Core Team (2013). R: A language and environment for statistical computing. R Foundation for Statistical Computing, Vienna, Austria. ISBN 3-900051-07-0, URL http://www.R-project.org/.

Rardin, M.J., Schilling, B., Cheng, L.Y., MacLean, B.X., Sorensen, D.J., Sahu, A.K., MacCoss, M.J., Vitek, O., Gibson, B.W. (2015). MS1 Peptide Ion Intensity Chromatograms in MS2 (SWATH) Data Independent Acquisitions. Improving Post Acquisition Analysis of Proteomic Experiments. Mol Cell Proteomics *14*: 2405–2419.

Schilling, B., Christensen, D., Davis, R., Sahu, A.K., Hu, L.I., Walker-Peddakotla, A., Sorensen, D.J., Zemaitaitis, B., Gibson, B.W., Wolfe, A.J. (2015). Protein acetylation dynamics in response to carbon overflow in Escherichia coli. Mol Microbiol *98*: 847–863.

Schilling, B., Gibson, B.W., Hunter, C.L. (2017). Generation of High-Quality SWATH(R) Acquisition Data for Label-free Quantitative Proteomics Studies Using TripleTOF(R) Mass Spectrometers. Methods Mol Biol *1550*: 223–233.

Schilling, B., Rardin, M.J., MacLean, B.X., Zawadzka, A.M., Frewen, B.E., Cusack, M.P., Sorensen, D.J., Bereman, M.S., Jing, E., Wu, C.C., Verdin, E., Kahn, C.R., Maccoss, M.J., Gibson, B.W. (2012). Platform-independent and label-free quantitation of proteomic data using MS1 extracted ion chromatograms in skyline: application to protein acetylation and phosphorylation. Mol Cell Proteomics *11*: 202–214.

Shilov, I.V., Seymour, S.L., Patel, A.A., Loboda, A., Tang, W.H., Keating, S.P., Hunter, C.L., Nuwaysir, L.M., Schaeffer, D.A. (2007). The Paragon Algorithm, a next generation search engine that uses sequence temperature values and feature probabilities to identify peptides from tandem mass spectra. Mol Cell Proteomics *6*: 1638–1655.

Taylor, S., Wakem, M., Dijkman, G., Alsarraj, M., and Nguyen, M. (2010). A practical approach to RT-qPCR—Publishing data that conform to the MIQE guidelines. Methods *50*, S1–S5.

Warnes, G.R., Bolker, B., Bonebakker, L., Gentleman, R., Huber,W., Liaw, A., Lumley, T., Maechler, M., Magnusson, A., Moeller, S., Schwartz, M., Venables, B. (2016) gplots: Various R programming tools for plotting data. R package version 3.0.1, URL https://cran.r-project.org/package=gplots.